Inorg. Chem. **2005**, *44*, 3016–3030

Reduction Pathway of End-On Terminally Coordinated Dinitrogen. IV. Geometric, Electronic, and Vibrational Structure of a W(IV) Dialkylhydrazido Complex and Its Two-Electron-Reduced Derivative Undergoing N–N Cleavage upon Protonation

Kay H. Horn, Natascha Böres, Nicolai Lehnert, Klaus Mersmann, Christian Näther, Gerhard Peters, and Felix Tuczek*

Institut für Anorganische Chemie der Christian-Albrechts-Universität Kiel, D-24098 Kiel, Germany

Received September 22, 2004

The molybdenum and tungsten dialkylhydrazido complexes $[M(dppe)_2(NNC_5H_{10})]^{2+}$ (M = Mo, W; compounds $\mathbf{A}^{Mo}$ and $\mathbf{A}^{W}$) and their two-electron-reduced counterparts $[M(dppe)_2(NNC_5H_{10})]$ (compounds $\mathbf{B}^{Mo}$ and $\mathbf{B}^{W}$) are characterized structurally and spectroscopically. The crystal structure of $\mathbf{B}^{W}$ indicates a geometry between square pyramidal and trigonal bipyramidal with the NNC_5H_{10} group in the apical position and in the trigonal plane of the complex, respectively. Temperature-dependent ^{31}P NMR spectra of $\mathbf{B}^{Mo}$ show that this geometry is present in solution as well. At room temperature, rapid Berry pseudorotation between the "axial" and "equatorial" ligand positions gives rise to a singlet in the ^{31}P NMR spectrum. This exchange process is slowed at low temperature, leading to a doublet. The N–N distance of $\mathbf{B}^{W}$ is 1.388 Å, and the W–N distance is 1.781 Å. Infrared and Raman spectroscopy applied to $\mathbf{A}^{W}$, $\mathbf{B}^{W}$, and their ^{15}N isotopomers reveals extensive mixing between the N–N and W–N vibrations of the metal–N–N core with the modes of the piperidine ring. The N–N force constant of $\mathbf{A}^{W}$ is determined to be 6.95 mdyn/A, which is close to the values of the Mo and W NNH_2 complexes. In $\mathbf{B}^{W}$, the N–N force constant decreases to 6.4 mdyn/Å, which is between the values found for the Mo/W NNH_3 and NNH_2 complexes. This allows us to attribute N–N double bond character to $\mathbf{A}^{W}$ and intermediate character between the double and single bonds for the N–N bond of $\mathbf{B}^{W}$. These findings are supported by DFT calculations. More importantly, the HOMO of $\mathbf{B}^{W}$ corresponds to a linear combination of the metal d_σ orbital with a ligand orbital having N–N σ^* character, inducing a weakening of the N–N bond. This contributes to the cleavage of the N–N bond taking place upon protonation of $\mathbf{B}^{W}$ at the N_β atom of the NNC_5H_{10} group.

I. Introduction

The catalytic conversion of N_2 to NH_3 on a sterically shielded Mo(III) triamidoamine complex has revealed new perspectives for the artificial reproduction of biological nitrogen fixation.[1] Not accidentally, the reactive pathway determined for this novel system shows close similarities to that known for the reduction and protonation of N_2 at Mo and W complexes with phosphine coligands. As is evident from Scheme 1, the conversion of dinitrogen to ammonia in these systems can be divided into two stages: (i) the protonation of end-on terminally coordinated N_2, leading to NNH, NNH_2, and NNH_3 species and (ii) the protonation of the nitrido complex, leading to NH_3. In the course of a catalytic reaction, six electrons are supplied along this path; the cycle is closed by the liberation of NH_3 and the rebinding of N_2. For the "classic" Mo/W phosphine systems, three catalytic cycles have been achieved.[2] In the Mo triamidoamine system, this number could be increased to six, with a much higher yield.[1] Between stages i and ii, the N−N bond is cleaved, generating the first molecule of NH_3. The

* To whom correspondence should be addressed. E-mail: ftuczek@ac.uni-kiel.de.

(1) (a) Yandulov, D. V.; Schrock, R. R. *Science* **2003**, *301*, 76. (b) Yandulov, D. V.; Schrock, R. R. *J. Am. Chem. Soc.* **2002**, *124*, 6252. (c) Ritleng, V.; Yandulov, D. V.; Weare, W. W.; Schrock, R. R.; Hock, A. S.; Davis, W. M.; *J. Am. Chem. Soc.* **2004**, *126*, 6150. (d) Yandulov, D. V.; Schrock, R. R.; Rheingold, A. L.; Cecciavelli, C.; Davis, W. M. *Inorg. Chem.* **2003**, *42*, 796.

(2) Pickett, C. J.; Talarmin, J. *Nature* **1985**, *317*, 652.

10.1021/ic048675g CCC: $30.25
Published on Web 02/23/2005

Scheme 1

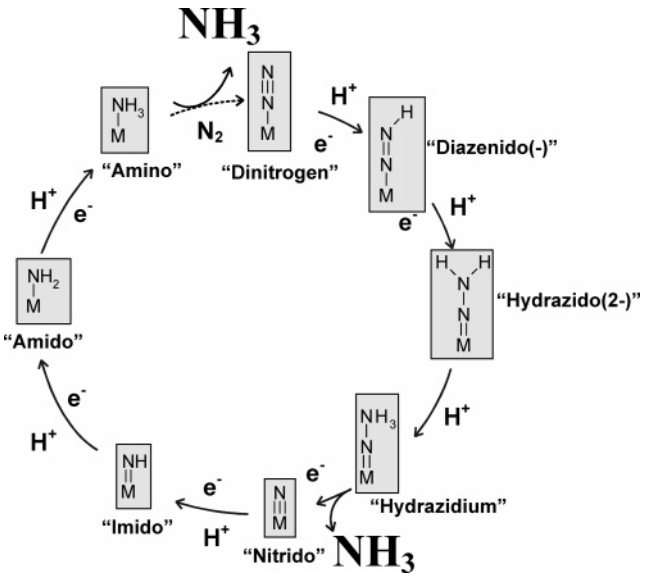

mechanism of this step is the subject of the present and follow-up paper.

To obtain insight into the electronic−structural factors influencing the activation of N_2 and its transition-metal-centered conversion to NH_3, we have studied the N_2 and NNH_x ($x = 1-3$) intermediates with the help of vibrational and optical spectroscopy coupled to DFT calculations.[3] A quantum chemistry-assisted normal coordinate analysis (QCA-NCA) has been developed for the evaluation of vibrational data, which is based on the calculation of the *f* matrix by DFT, followed by simplification of this matrix to the largest matrix elements and subsequent fitting of important force constants to match experimentally observed frequencies. Using this methodology, we have investigated, in particular, the N_2, N_2H, and N_2H_2 complexes $[W(N_2)_2(dppe)_2]$, $[WF(NNH)(dppe)_2]$, and $[WF(NNH_2)(dppe)_2]^+$; dppe = 1,2-bis(diphenylphosphino)ethane).[3a,b] More recently, these studies were complemented by the investigation of Mo and W hydrazidium complexes with depe coligands $[MF(NNH_3)(depe)_2](BF_4)_2$, M = Mo and W (depe = 1,2-bis(diethylphosphinoethane)).[3c]

Upon conversion of, for example, $[W(N_2)_2(dppe)_2]$ to the NNH complex $[WF(NNH)(dppe)_2]$, the N−N force constant decreases from about 16 mdyn/Å to a value of 8.27 mdyn/Å, and the M−N force constant increases from a value of about 2.5 to 4.5 mdyn/Å. This trend continues in the next protonation steps; that is, for $[WF(NNH_2)(dppe)_2]^+$, the N−N force constant is reduced further to a value of 7.2 mdyn/Å, and the metal−N force constant is increased further to 6.3 mdyn/Å. In the NNH_3 complexes $[MF(NNH_3)(depe)_2]^{2+}$, M = Mo or W, the N−N force constant is found to be 6.03 mdyn/Å, which is close to the value of an N−N single bond, whereas the metal−N force constants (8.01 and 7.31 mdyn/Å, respectively) reach values that are typical for a metal−N triple bond. The decrease of the N−N force constants upon stepwise protonation indicates a successive reduction of N−N bond order, thus initiating bond cleavage, whereas the increase of the metal−N force constants reflects a successive strengthening of the metal−N bond. Besides providing an energetic driving force for the reduction of the N−N triple bond, this also acts to prevent the loss of the partially reduced NNH_x substrate, $x = 1-3$, in the course of the transformation of N_2 to ammonia.

The ultimate stage of N_2 reduction and protonation at d^6 metal centers in the absence of external reductants is thus reached in Mo(IV)/W(IV) hydrazidium complexes. If the phosphine coligands remain bound to the metal center, then these compounds are stable toward N−N splitting in solution. This is supported by a theoretical simulation of the heterolytic N−N cleavage of $[MoF(NNH_3)(PH_3)_4]^+$, leading to NH_3 and the Mo(VI) nitrido complex $[MoF(N)(PH_3)_4]^{2+}$, which indicates that this process is endothermic ($\Delta H = +40$ kcal/mol, $\Delta G = +30$ kcal/mol).[3c] Splitting of the N−N single bond therefore requires the transfer of electrons from an external source. Because NNH_3^- compounds are strongly acidic,[2c] this reduction is performed better at the NNH_2 stage. Subsequent protonation of the two-electron-reduced intermediate then leads to a Mo(II) hydrazidium intermediate, which in turn mediates N−N cleavage. The transition-metal-mediated reaction of N_2 to the first molecule of ammonia thus involves three steps: (1) reduction of the N−N triple bond to a double bond by addition of the first proton, leading to the NNH complex, (2) protonation of the NNH complex to the NNH_2 complex that still has an N−N double bond, and (3) two-electron reduction and further protonation of the NNH_2 complex, leading to a doubly reduced NNH_3 complex that undergoes splitting of its N−N single bond.

Mechanistic insight into the N−N cleavage process is obtained favorably using alkylated (NNR_2) derivatives,[4−6] Thus, protonation of the five-coordinate complex $[Mo(NNC_5H_{10})(dppe)_2]$ (compound $\mathbf{B}^{Mo}$) with HBr in THF leads to N−N splitting under the formation of HNC_5H_{10} (piperidine) and the imido complex $[MoBr(NH)(dppe)_2]Br$. Compound $\mathbf{B}^{Mo}$ has been generated by treatment of the Mo(IV) dialkylhydrazido(2-) complex $[MoBr(NNC_5H_{10})(dppe)_2]Br$ (compound $\mathbf{A}^{Mo}$) with BuLi or electrochemically at −1.61 V versus SCE.[7] Compound $\mathbf{A}^{Mo}$ in turn is accessible by the alkylation of $[M(N_2)_2(dppe)_2]$ with α,ω-dibromopentane in a photoreaction.

Here, the synthesis and the spectroscopic and theoretical characterization of $\mathbf{A}^{Mo}$, $\mathbf{B}^{Mo}$, and their tungsten analogues, $\mathbf{A}^{W}$ and $\mathbf{B}^{W}$, respectively, are presented. A single-crystal X-ray structure determination of compound $\mathbf{B}^{W}$ is reported, and the variable-temperature ^{31}P NMR spectra of $\mathbf{B}^{Mo}$ are interpreted. Furthermore, the vibrational properties of compounds $\mathbf{A}^{W}$ and $\mathbf{B}^{W}$ are evaluated. Infrared and Raman data are analyzed using the QCB-NCA procedure, which is an

(3) (a) Lehnert, N.; Tuczek, F. *Inorg. Chem.* **1999**, *38*, 1659. (b) Lehnert, N.; Tuczek, F. *Inorg. Chem.* **1999**, *38*, 1671. (c) Horn, K. H.; Lehnert, N.; Tuczek, F. *Inorg. Chem.* **2003**, *42*, 1076. (d) Tuczek, F.; Horn, K. H.; Lehnert, N. *Coord. Chem. Rev.* **2003**, *245*, 107.

(4) Pickett, C. J.; Leigh, G. J. *J. Chem. Soc., Chem. Commun.* **1981**, 1033.

(5) Hussain, W.; Leigh, G. J.; Pickett, C. J. *J. Chem. Soc., Chem. Commun.* **1982**, 747.

(6) Henderson, R. A.; Leigh, G. J.; Pickett, C. J. *J. Chem. Soc., Dalton Trans.* **1989**, 425

(7) Ferrocene at 0.55 V under these conditions

improved version of QCA-NCA,[8] making use of the full *f* matrix generated by DFT. This method is useful particularly for the spectroscopic analysis of systems exhibiting a complex vibrational structure. Finally, the electronic structure of compounds $\mathbf{A}^{M}$ and $\mathbf{B}^{M}$ (M = Mo, W) is evaluated using DFT, with special emphasis on the nature of the frontier orbitals. In the following paper, the protolytic N−N cleavage of compound $\mathbf{B}^{W}$ is investigated both spectroscopically and theoretically. This paper also presents a DFT analysis of the N−N splitting process in the sterically shielded Mo(triamidoamine) dinitrogen complex. The reaction pathways of both systems mediating the N−N cleavage of end-on terminally bound dinitrogen are compared to each other, and the implications with respect to transition-metal-centered reduction of N_2 to NH_3 are discussed.

II. Experimental and Computational Procedures

Sample Preparation, Isotopic Substitution. The reactions and sample preparations were performed under a nitrogen or argon atmosphere using Schlenk techniques. Sample manipulations for vibrational spectroscopy were carried out in a glovebox. All solvents were dried under argon. Sample preparation was carried out following literature procedures.[5,9] The alkylhydrazido complexes [MBr(NNC$_5$H$_{10}$)(dppe)$_2$]Br ($\mathbf{A}^{M}$, M = Mo, W) were obtained by the photoreaction of [M(N$_2$)$_2$(dppe)$_2$] in the presence of 1,5-dibromopentane. The ^{15}N-labeled compounds were prepared using the corresponding isotope-labeled dinitrogen complexes [M(^{15}N)$_2$(dppe)$_2$]. The **A** compounds were reduced with BuLi under reductive elimination of the trans ligand, forming the reduced intermediates [M(NNC$_5$H$_{10}$)(dppe)$_2$] ($\mathbf{B}^{M}$; M = Mo, W). Protonation of these intermediates leads to N−N cleavage and the generation of 1 equiv of piperidine (cf. the following paper).

IR Spectroscopy. Middle-infrared **(**MIR) spectra were obtained from KBr pellets using a Mattson Genesis Type I spectrometer. Far-infrared (FIR) spectra were obtained from RbI pellets using a Bruker IFS 66s FTIR spectrometer. Both instruments are equipped with a Cryogenic (CTI) helium cryostat. The spectra were recorded at 10 K, and the resolution was set to 2 cm^{-1}.

NMR Spectroscopy. NMR spectra were recorded on a Bruker Avance 400 pulse Fourier transform spectrometer operating at a ^{1}H frequency of 400.13 MHz using a 5-mm inverse triple-resonance probe head. Reference: H_3PO_4 85% pure $\delta(^{31}P) = 0$ ppm.

X-ray Structure Analysis of $\mathbf{B}^{W}$. Intensity data were collected using a STOE imaging plate diffraction system with Mo Kα radiation. The structures were solved with direct methods using SHELXS-97,[10] and refinement was performed against F^2 using SHELXL-97.[10] All of the non-H atoms were refined anisotropically. The hydrogen atoms were positioned with idealized geometry and refined with isotropic displacement parameters using a riding model. Details of the structure analysis are collected in Table 1.

Normal Coordinate Analysis. Normal coordinate calculations were performed using the QCPE computer program 576 by M. R. Peterson and D. F. McIntosh. It involves the solution of the secular equation $\mathbf{GFL} = \Lambda\mathbf{L}$ by the diagonalization procedure of Miyazawa.[11] The calculations are based on a general valence force field, and the force constants are refined using the nonlinear optimization routine of the simplex algorithm according to Nelder and Mead.[12] Normal coordinate analysis is based on the QCB-NCA procedure that involves the generation of an initial force field by DFT methods.[8] For the alkylhydrazido complexes [WBr(NNC$_5$H$_{10}$)(dppe)$_2$]Br ($\mathbf{A}^{W}$) and [W(NNC$_5$H$_{10}$)(dppe)$_2$] ($\mathbf{B}^{W}$), models [MoBr(NNC$_5$H$_{10}$)(PH$_2$C$_2$H$_4$PH$_2$)$_2$]$^+$ (**$\tilde{A}$**) and [Mo(NNC$_5$H$_{10}$)(PH$_2$C$_2$H$_4$PH$_2$)$_2$] (**$\tilde{B}$**) were employed for DFT calculations, giving the theoretical frequencies and the matrix of the force constants, $\tilde{f}$ (see below). Hydrogens at the P atoms were removed to eliminate interactions between the PH$_2$ groups and the rest of the molecule, leading to model systems [MoBr(NNC$_5$H$_{10}$)(PC$_2$H$_4$P)$_2$]$^+$ (**A′**) and [Mo(NNC$_5$H$_{10}$)(PC$_2$H$_4$P)$_2$] (**B′**), which were then used for NCA. The complete *f* matrix is extracted from the DFT calculation and taken as the initial guess. Relevant force constants are then modified.

DFT Calculations. Spin-restricted DFT calculations were performed for the model complexes [MoBr(NNC$_5$H$_{10}$)(PH$_2$C$_2$H$_4$PH$_2$)$_2$]$^+$ (**$\tilde{A}$**) and [Mo(NNC$_5$H$_{10}$)(PH$_2$C$_2$H$_4$PH$_2$)$_2$] (**$\tilde{B}$**) using Becke's three-parameter hybrid functional with the correlation functional of Lee, Yang, and Parr (B3LYP).[13] The LANL2DZ basis set was used for the calculations. It applies Dunning/Huzinaga full double-ζ (D95)[14] basis functions on the first row and Los Alamos effective

Table 1. Parameters for $\mathbf{B}^{W}$

a. X-Ray Structure Determination

compound	**I**
empirical formula	$C_{57}H_{29}N_2P_4W$
fw (g·mol^{-1})	1078.79
cryst syst	triclinic
space group	$P\bar{1}$
a (Å)	12.645(1)
b (Å)	12.936(1)
c (Å)	16.781(2)
α (deg)	84.98(1)
β (deg)	76.41(1)
γ (deg)	67.18(1)
V (Å^3)	2459.2(4)
temp (K)	180
Z	4
D_{calcd} (g·cm^{-3})	1.457
2*θ* range	3−50°
μ(Mo Kα) (mm^{-1})	2.52
measured refln	16045
R_{int}	0.0652
independent refln	8020
refln with $I > 2\sigma(I)$	6467
refined params	621
$R_1[I > 2\sigma(I)]$	0.0423
wR2 (all data)	0.0989
GOF	1.006
min/max res/e·Å^{-3}	0.94/−1.31

b. Bond Distances and Angles

W(1)−N(2)	1.781(5)	W(1)−P(2)	2.3961(2)
W(1)−P(3)	2.4195(2)	W(1)−P(1)	2.4346(2)
W(1)−P(4)	2.4682(2)		
N(1)−N(2)	1.388(7)	N(1)−C(95′)	1.452(7)
N(1)−C(95)	1.45(2)	N(1)−C(91)	1.46(2)
N(2)−W(1)−P(2)	126.3(2)	N(2)−W(1)−P(3)	125.9(2)
P(2)−W(1)−P(3)	107.7(1)	N(2)−W(1)−P(1)	99.3(2)
P(2)−W(1)−P(1)	77.8(1)	P(3)−W(1)−P(1)	87.9(1)
N(2)−W(1)−P(4)	103.6(2)	P(2)−W(1)−P(4)	89.7(1)
P(3)−W(1)−P(4)	77.6(1)	P(1)−W(1)−P(4)	157.1(1)

(8) Studt, F.; MacKay, B. A.; Fryzuk, M. D.; Tuczek, F. *J. Am. Chem. Soc.* **2004**, *126*, 280.
(9) Chatt, J.; Hussain, W.; Leigh, G. J.; Terreros, F. P. *J. Chem. Soc., Dalton Trans.* **1980**, 1408.
(10) Sheldrick, G. M. *SHELXS-97 and SHELXL-97: Program for the Solution and Refinement of Crystal Structures*; University of Göttingen: Göttingen, Germany, 1997.
(11) Miyazawa, T. J. *Chem. Phys.* **1958**, *29*, 246.
(12) Nelder, J. A.; Mead, R. *Comput. J.* **1965**, *7*, 308.
(13) Becke, A. D. *J. Chem. Phys.* **1993**, *98*, 5648.
(14) Dunning, T. H., Jr.; Hay, P. J. In *Modern Theoretical Chemistry*; Schaefer, H. F., III, Ed.; Plenum: New York, 1976.

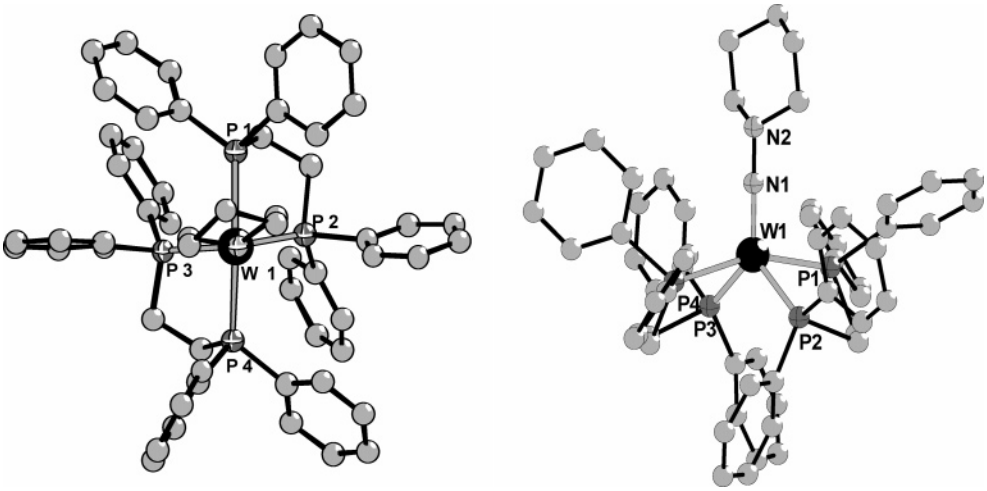

Figure 1. Structure of the tungsten analogue of compound $\mathbf{B}^{W}$ [$W(NNC_5H_{10})(dppe)_2$] with labeling. Views down the $N_2-N_1-W_1$ axis (left) and onto the $W_1-N_1-N_2$ axis (right). H atoms are omitted for clarity.

core potentials plus DZ functions on all of the other atoms.[15] Charges are analyzed using the natural bond orbital (NBO) formalism (natural population analysis, NPA).[16] All of the computational procedures are used as they are implemented in the Gaussian 98 package.[17] Wave functions are plotted with the visualization program Molden.[18] The *f* matrix in internal coordinates is extracted from the Gaussian output using the program Redong.[19] Vibrational frequencies were calculated by DFT on the basis of the fully optimized molecules.

III. Results and Analysis

A. X-ray Structural and NMR Spectroscopic Characterization of [M(NNC$_5$H$_{10}$)(dppe)$_2$] (M = Mo, W). [$W(NNC_5H_{10})(dppe)_2$] (compound $\mathbf{B}^{W}$) crystallizes in the triclinic space group $P\bar{1}$ with two formula units in the unit cell and all of the atoms located in general positions. The structure of the complex molecule is given in Figure 1 with views down the $N_2-N_1-W_1$ axis (left) and onto the $W_1-N_1-N_2$ axis (right); H atoms are omitted for clarity. Important bond lengths and angles are collected in Table 1. The W atom is coordinated by four P atoms of two dppe ligands and one N atom of the nitrogen ligand in a distorted trigonal-bipyramidal geometry with P1 and P4 in axial positions and P2, P3, and N2 in equatorial positions. The N−W−P angles in the equatorial plane are approximately 126° (N1−W1−P3: 125.9 (2)°, N1−W1−P2: 126.3 (2)°), whereas the N−W−P angles to the axial phosphines are 103.6 (2)° (N1−W1−P4) and 99.3 (2)° (N1−W1−P1). The angle between the axial P atoms is larger (157.1 (1)°) than that between P atoms in the equatorial plane (107.7 (1)°), in agreement with the approximate trigonal-bipyramidal geometry of the complex. The W atom is located 0.040(2) Å above the trigonal plane. W−P bond lengths scatter between 2.3961(2) and 2.4682(2) Å and are in the normal range observed for such compounds. The N−N distance of 1.388(7) Å is significantly larger than that found in tungsten "hydrazido(2-)" complexes (around 1.33 Å)[20] but is somewhat shorter than that in a structurally characterized W hydrazidium (NNH_3^-) complex (1.396 Å).[21] The N1−N2(C)−C group is distinctly nonplanar, indicative of some sp^3 character of the terminal N atom. With 1.781(5) Å, the W−N distance has about the same value as in the mentioned W hydrazidium complex (1.785 Å) but is longer than in a Mo−NNH_2−dppe compound (1.763 Å).[22] Additional data is available in the Supporting Information.

The ^{31}P NMR spectrum of [$Mo(NNC_5H_{10})(dppe)_2$] in THF/pentane shows a single sharp peak at room temperature, in agreement with the literature (Figure 2).[23] This peak is found to remain unsplit down to 243 K (δ = 86.8 ppm).[24] Upon further temperature decrease, the peak broadens and at 203 K is split into two signals centered at 86.5 and 85.6 ppm. From the crystal structure information, this can be interpreted as being due to the freezing of a Berry pseudorotation of the phosphine groups between the equatorial and axial positions. Both peaks are resolved into triplets, corresponding

(15) (a) Hay, P. J.; Wadt, W. R. *J. Chem. Phys.* **1985**, *82*, 270 and 299. (b) Wadt, W. R.; Hay, P. J. *J. Chem. Phys.* **1985**, *82*, 284.
(16) (a) Foster, J. P.; Weinhold, F. *J. Am. Chem. Soc.* **1980**, *102*, 7211. (b) Rives, A. B.; Weinhold F. *Int. J. Quantum Chem.* **1980**, *14*, 201. (c) Reed, A. E.; Weinstock, R. B.; Weinhold, F. *J. Chem. Phys.* **1985**, *83*, 735. (d) Reed, A. E.; Curtiss, L. A.; Weinhold, F. *Chem. Rev.* **1988**, *88*, 899.
(17) Frisch, M. J.; Trucks, G. W.; Schlegel, H. B.; Scuseria, G. E.; Robb, M. A.; Cheeseman, J. R.; Zakrzewski, V. G.; Montgomery, J. A., Jr.; Stratmann, R. E.; Burant, J. C.; Dapprich, S.; Millam, J. M.; Daniels, A. D.; Kudin, K. N.; Strain, M. C.; Farkas, O.; Tomasi, J.; Barone, V.; Cossi, M.; Cammi, R.; Mennucci, B.; Pomelli, C.; Adamo, C.; Clifford, S.; Ochterski, J.; Petersson, G. A.; Ayala, P. Y.; Cui, Q.; Morokuma, K.; Malick, D. K.; Rabuck, A. D.; Raghavachari, K.; Foresman, J. B.; Cioslowski, J.; Ortiz, J. V.; Stefanov, B. B.; Liu, G.; Liashenko, A.; Piskorz, P.; Komaromi, I.; Gomperts, R.; Martin, R. L.; Fox, D. J.; Keith, T.; Al-Laham, M. A.; Peng, C. Y.; Nanayakkara, A.; Gonzalez, C.; Challacombe, M.; Gill, P. M. W.; Johnson, B. G.; Chen, W.; Wong, M. W.; Andres, J. L.; Head-Gordon, M.; Replogle, E. S.; Pople, J. A. *Gaussian 98*, revision A.7; Gaussian, Inc.: Pittsburgh, PA, 1998.
(18) Schaftenaar, G. *Molden*, version 3.2; CAOS/CAMM Center, University of Nijmegen: Nijmegen, The Netherlands.
(19) Allouche, A.; Pourcin, J. *Spectrochim. Acta* **1993**, *49A*, 571.
(20) Hidai, M.; Kodama, T.; Sato, M.; Harakawa, M.; Uchida, Y. *Inorg. Chem.* **1976**, *15*, 2694.
(21) (a) Galindo, A.; Hills, A.; Hughes, D. L.; Richards, R. L. *J. Chem. Soc., Dalton Trans.* **1990**, 283. (b) Galindo, A.; Hills, A.; Hughes, D. L.; Richards, R. L. *J. Chem. Soc., Chem. Commun.* **1987**, 1815.
(22) Hidai, M.; Kodama, T.; Sato, M.; Harakawa, M.; Uchida, Y. *Inorg. Chem.* **1976**, *15*, 2694.
(23) (b) Henderson, R. A.; Leigh, G. J.; Pickett, C. *Adv. Inorg. Chem. Radiochem.* **1983**, *27*, 197−292.
(24) Chemical shifts are referenced to H_3PO_4.

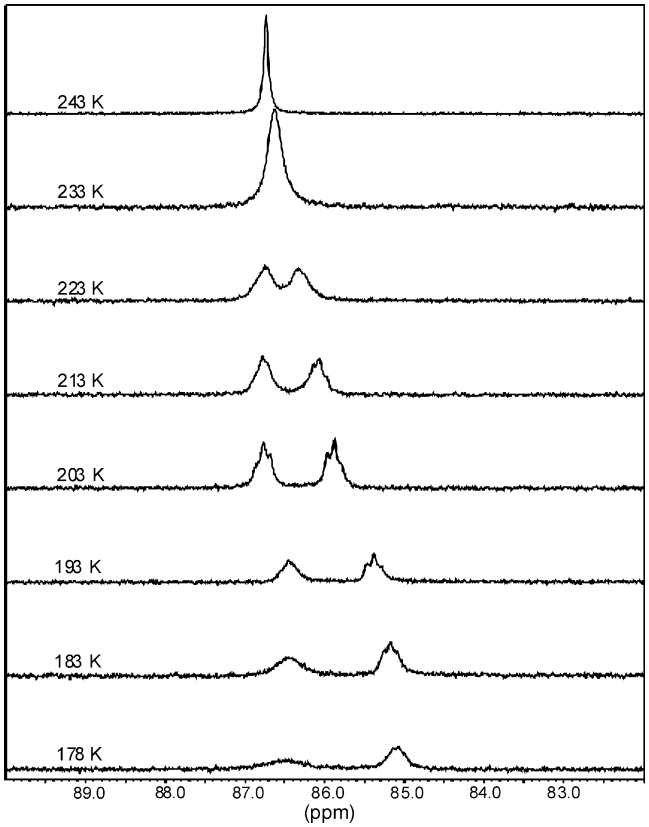

Figure 2. Variable-temperature NMR spectra of $\mathbf{B}^{Mo}$.

to a coupling between two equatorial and two axial phosphines. At even lower temperature, a broadening of the low-field peak is observed, possibly reflecting the onset of a nonequivalence of the two axial phosphine positions. This might be associated with the pyramidal geometry of the terminal NR_2 group where the direction of, for example, the lone pair at N_β can be "up" (i.e., in the direction of P1) or "down" (i.e., in the direction of P4). Rapid flipping between these two positions would then lead to the unsplit low-field peak of the doublet that is observed at higher temperatures. The temperature dependence of the ^{31}P NMR spectrum thus reflects both the trigonal-pyramidal geometry of the complex (as opposed to a quadratic-pyramidal configuration suggested by the room-temperature singlet) and the pyramidal configuration of N_β, indicating some sp^3 character of this atom and single-bond character of the N−N bond, respectively.

B. Vibrational Spectroscopic Analysis. 1. Vibrational Spectrum of Piperidine. For the infrared and Raman spectral analysis of the alkylated complexes $\mathbf{A}^W$ and $\mathbf{B}^W$, the vibrational spectrum of piperidine was calculated. The force constants of the H−C−H bends were reduced by 10%, and those of the H−C−C/H−C−N bends were reduced by 5% to reproduce the experimental spectrum optimally in the range between 1500 and 500 cm^{-1}. Analogous modifications were applied in the QCB-NCA of compounds $\mathbf{A}^W$ and $\mathbf{B}^W$. The experimental gas-phase spectrum of piperidine[25] is compared to the calculated IR spectrum with adjusted force constants in Figure 3, showing excellent agreement between

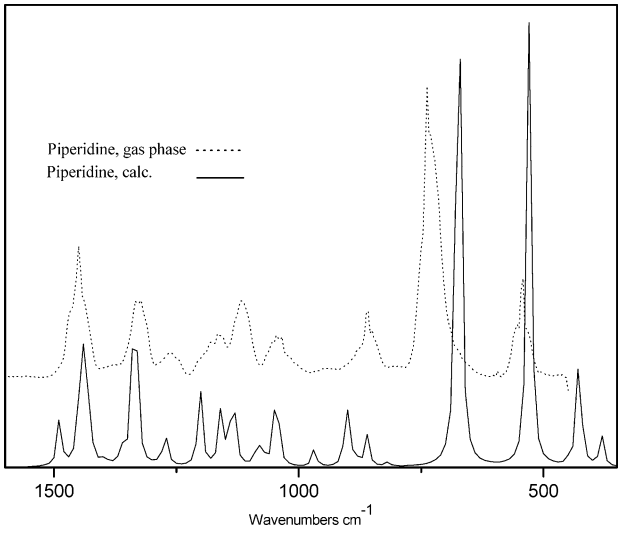

Figure 3. Experimental and calculated IR spectra of piperidine.

theory and experiment. The calculated frequencies of the 45 normal vibrations of piperidine, $\nu_1-\nu_{45}$, are given along with their primary character in Table 2. At the highest frequency, the N−H stretch ν_1 is found (3540 cm^{-1}). The 10 C−H stretching vibrations are located in the region between 3100 and 2900 cm^{-1}; at lower energy, the H−C−H scissoring vibrations $\delta(HCH)_{sc}$ are found. The five "wagging" and five "twisting" modes of the CH_2 groups are calculated in frequency ranges between 1428 and 1351 cm^{-1} ($\delta(HCH)_{wag}$) and between 1335 and 1159 cm^{-1} ($\delta(HCH)_{twist}$), respectively. The H−N−C bending modes δ(HNC) are distributed over the vibrations ν_{16}, ν_{17}, ν_{18}, ν_{20}, and ν_{22}.

At lower energy, C−N and C−C stretches are located. The antisymmetric C−N vibration $\nu_{26} = \nu_{as}$(CN) is calculated at 1201 cm^{-1}. Two C−C stretching modes (ν_{29} and ν_{30}) are found at 1134 and 1084 cm^{-1}; other C−C stretches combine with stretches of the C−N−C unit at 902 cm^{-1} (ν_{34}) and 885 cm^{-1} (ν_{35}), and the totally symmetric stretching vibration of the ring is at 817 cm^{-1} (ν_{38}). The five H−C−H "rocking" modes are distributed over a region between 1156 and 529 cm^{-1}. Different combinations of C−C−C− with C−N−C− bending modes are calculated at 1071, 1045, 446, and 427 cm^{-1}. Torsions (τ) around the C−C and C−N bonds mark the low-energy end of the spectrum.

2. Spectral Analysis of $\mathbf{A}^W$. MIR and FIR spectra of [WBr(NNC_5H_{10})$(dppe)_2$]Br ($\mathbf{A}^W$) and [WBr($^{15}N^{15}NC_5H_{10}$)-$(dppe)_2$]Br ($^{15}N-\mathbf{A}^W$), including all relevant isotopic shifts, are presented in Figure 4. Experimental and calculated frequencies are collected in Table 3. Comparison of the IR spectra of $^{14}N-\mathbf{A}^W$ and $^{15}N-\mathbf{A}^W$ indicates several isotope-sensitive bands in the MIR region, which are designated as Ia, Ib, II, III, and so forth. On the basis of a DFT frequency calculation (cf. Table 3), these features are assigned to combinations of the N−N− and W−N stretches, C−N/CC− stretching vibrations of the piperidine ring, and the in-plane bending motion of the linear W−N−N unit.

The N−N stretch itself is distributed over at least four bands (Ia, Ib, IV, and V). The peak at 1420 cm^{-1} (Ia) in the spectrum of $^{14}N-\mathbf{A}^W$ that shows an isotopic shift to 1412

(25) NIST Standard Reference Data Program Collection (C) 2003.

Table 2. Calculated Frequencies and Assignments for Free Piperidine[a]

	type	calcd		type	calcd		type	calcd
ν_1	ν(NH)	3540	ν_{16}	$\delta(HCH)_{sc}$	1438	ν_{31}	δ(CNC)/δ(CCC)	1071
ν_2	ν(CH)	3111	ν_{17}	$\delta(HCH)_{wag}$	1428	ν_{32}	δ(CNC)/δ(CCC)	1045
ν_3	ν(CH)	3102	ν_{18}	$\delta(HCH)_{wag}$	1396	ν_{33}	$\delta(HCH)_{rock}$	968
ν_4	ν(CH)	3093	ν_{19}	$\delta(HCH)_{wag}$	1362	ν_{34}	ν(CC)/ν(CN)	902
ν_5	ν(CH)	3087	ν_{20}	$\delta(HCH)_{wag}$	1356	ν_{35}	ν(CC)/ν(CN)	885
ν_6	ν(CH)	3084	ν_{21}	$\delta(HCH)_{wag}$	1351	ν_{36}	$\delta(HCH)_{rock}$	860
ν_7	ν(CH)	3045	ν_{22}	$\delta(HCH)_{tw}$	1335	ν_{37}	$\delta(HCH)_{rock}$	818
ν_8	ν(CH)	3044	ν_{23}	$\delta(HCH)_{tw}$	1293	ν_{38}	ν(CC)/ν(CN)	817
ν_9	ν(CH)	3024	ν_{24}	$\delta(HCH)_{tw}$	1275	ν_{39}	δ(CNC)/$\delta(HCH)_{rock}$	673
ν_{10}	ν(CH)	2917	ν_{25}	$\delta(HCH)_{tw}$	1269	ν_{40}	δ (CCC)/$\delta(HCH)_{rock}$	529
ν_{11}	ν(CH)	2910	ν_{26}	νas(CN)	1201	ν_{41}	δ(CCC)/δ(CNC)	446
ν_{12}	$\delta(HCH)_{sc}$	1488	ν_{27}	$\delta(HCH)_{tw}$	1159	ν_{42}	δ(CCC)/δ(CNC)	427
ν_{13}	$\delta(HCH)_{sc}$	1458	ν_{28}	$\delta(HCH)_{rock}$	1156	ν_{43}	τ^{CC}	381
ν_{14}	$\delta(HCH)_{sc}$	1444	ν_{29}	ν(CC)	1134	ν_{44}	τ^{CC}	246
ν_{15}	$\delta(HCH)_{sc}$	1443	ν_{30}	ν(CC)	1084	ν_{45}	τ^{CC}	235

[a] The H−C−H and H−C−C/H−C−N bending force constants have been reduced by 10 and 5%, respectively, to achieve optimal agreement with the gas-phase spectrum of piperidine (see text).

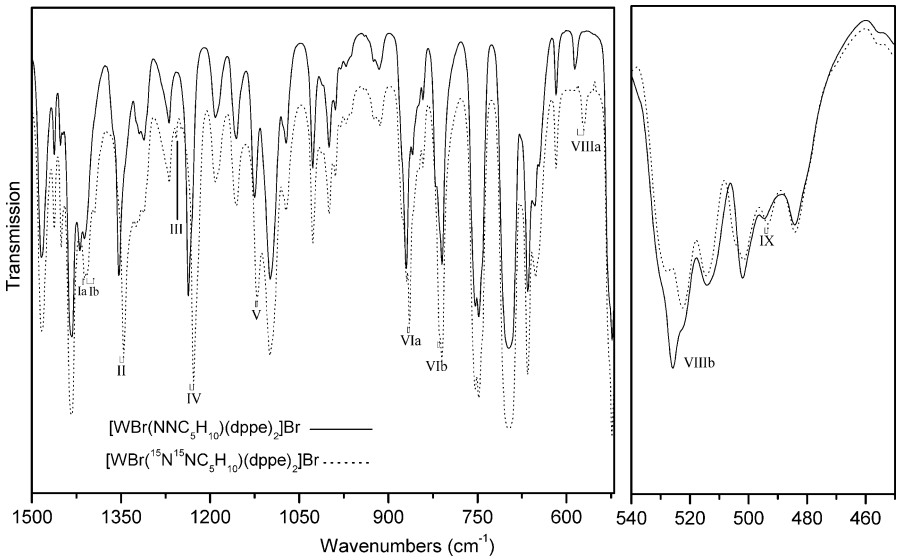

Figure 4. IR spectra of $[WBr(NNC_5H_{10})(dppe)_2]Br$ and $[WBr(^{15}N^{15}NC_5H_{10})(dppe)_2]Br$.

Table 3. Observed and Calculated Frequencies for $^{14}N-\mathbf{A}^W$ and $^{15}N-\mathbf{A}^W$

		exptl						
		IR		Raman		QCB-NCA		
band no.	main character	^{14}N	^{15}N	^{14}N	^{15}N	^{14}N	^{15}N	DFT
Ia	ν(NN) + ν_{12}: ***ν*(NN)[1]**	1420	1412	1418	1410	1416	1389	1481
Ib		1411	1395	1408	1393			1388
II	ν_{21} + ν(NN) + ν(CN)	1353	1345			1360	1356	1377
III	ν_{24} + ν(NN) + $\nu(CN)_{as}$		1258			1271	1269	1276
IV	ν_{25} + ν(NN): ***ν*(NN)[2]**	1236	1228	1237	1229	1236	1228	1260
V	ν_{28} + ν(NN): ***ν*(NN)[3]**	1125	1120	1126	1121	1135	1132	1163
VIa	ν_{35} + ν(WN)	874	864	870	861	866	860	879
VIb	ν_{38} + ν(WN)	820	814	821	813	807	799	817
VII	ν_{39}					624	621	644
VIIIa	δ^{ip}(WNN)	585	572			587	573	594
VIIIb	δ^{oop}(WNN)	525				521	506	506
IX	ν_{40} + ν(WN)	494	492			483	481	492

cm^{-1} in $^{15}N-\mathbf{A}^W$ is assigned to a combination of ν(NN) and the ν_{12} H−C−H bending mode of piperidine. A second component of ν(NN) combined with $\delta(HCH)_{wag}$ (ν_{18}) is found at 1411 cm^{-1} (Ib); this peak is shifted to 1395 cm^{-1} in $^{15}N-\mathbf{A}^W$. The ν_{21} H−C−H bending vibration is comparable to its position in free piperidine (1351 cm^{-1}) and is observed at 1353 cm^{-1} (1345 cm^{-1} in $^{15}N-\mathbf{A}^W$; band II). The antisymmetric C−N stretching vibration $\nu(CN)_{as}$ corresponding to ν_{26} of free piperidine is observed at 1258 cm^{-1} for $^{15}N-\mathbf{A}^W$ (band III); the counterpart of this vibration in the spectrum of $^{14}N-\mathbf{A}^W$ cannot be identified. The intense feature at 1236 cm^{-1} in the spectrum of $^{14}N-\mathbf{A}^W$ that shifts to 1228 cm^{-1} in $^{15}N-\mathbf{A}^W$ (band IV) is assigned to a combination of ν(NN) with the HCH twisting mode ν_{25}. At 1125 cm^{-1} with an isotopic shift to 1120 cm^{-1}, a combination of ν(NN) with ν_{28} is observed (band V). Between 900 and

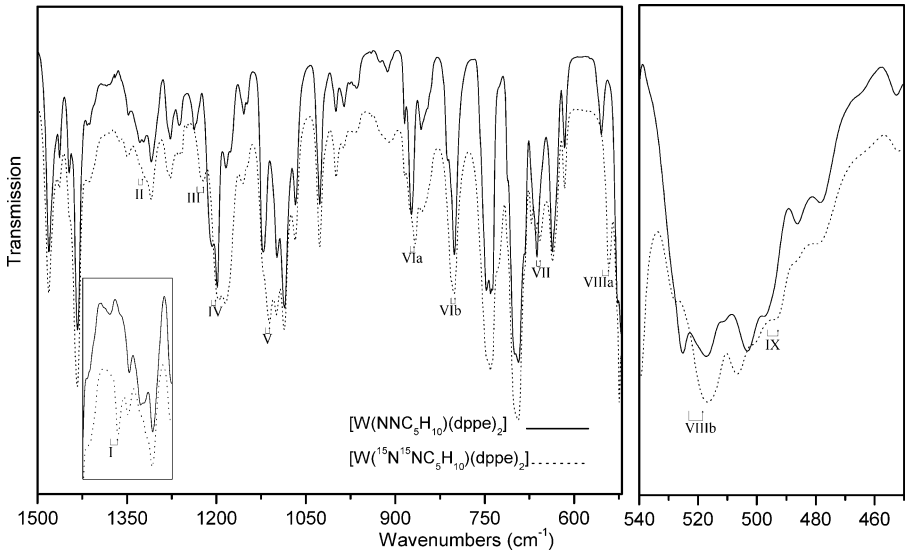

Figure 5. IR spectra of $[W(NNC_5H_{10})(dppe)_2]$ and $[W(^{15}N^{15}NC_5H_{10})(dppe)_2]$.

800 cm^{-1}, two isotope-sensitive bands (VIa and VIb) are found, which are assigned to a stretching vibration of the piperidine ring (ν_{35}) and a $\delta(HCH)_{rock}$ mode (ν_{38}), respectively, becoming isotope-sensitive because of an admixture of nitrogen motion. These findings are supported by Raman data (Figure S1 and Table 3). At the low-energy end, the MIR spectrum of $^{14}N-\mathbf{A}$ exhibits a band at 585 cm^{-1} (VIIIa) that shifts by about -13 cm^{-1} in the spectrum of $^{15}N-\mathbf{A}$ and is assigned to δ^{ip}(WNN). This vibration corresponds approximately to the bending motion of the W−N−N unit in the NCC plane of the piperidine ring. DFT predicts another isotope-sensitive band at 644 cm^{-1} (band VII); however, no such feature is observed in this region.

In the FIR spectrum of $\mathbf{A}^W$ ($\tilde{\nu}$ < 500 cm^{-1}), unequivocal assignment of the observed bands is difficult. From the DFT frequency calculation, the out-of-plane component of the WNN bend, δ^{oop}(WNN), is expected in this spectral region. This vibration is assigned to the band at 525 cm^{-1} (VIIIb), which disappears in the spectrum of the ^{15}N-labeled complex and is possibly superimposed by the broad feature at 514 cm^{-1}. The band at 492 cm^{-1} (IX) that shifts to 492 cm^{-1} on isotopic substitution is assigned to a combination of ν_{40} with ν(WN).

3. Spectral Analysis of $\mathbf{B}^W$. The IR spectra of $[W(NNC_5H_{10})(dppe)_2]$ ($^{14}N-\mathbf{B}^W$) and $[W(^{15}N^{15}NC_5H_{10})(dppe)_2]$ ($^{15}N-\mathbf{B}^W$) are presented with all of the relevant isotopic shifts in Figure 5. Table 4 comprises the observed and calculated frequencies along with the assignments. Spectral comparison of $^{14}N-\mathbf{B}^W$ and $^{15}N-\mathbf{B}^W$ indicates several isotope sensitive bands in the MIR region. They are assigned to N−N, W−N, and C−N stretching vibrations, a bending mode of the linear W−N−N unit, and ring vibrations of the piperidine moiety. Band designations (I, II, ...) are chosen by close analogy to $\mathbf{A}^W$.

Band I is observed at 1382 cm^{-1} in the spectrum of $^{14}N-\mathbf{B}^W$, shifting to 1366 cm^{-1} in the spectrum of $^{15}N-\mathbf{B}^W$. At 1329 cm^{-1} with an isotopic shift to 1321 cm^{-1}, ν_{21} (band II) is found. The feature at 1237 cm^{-1} that shifts to 1223 cm^{-1} in the ^{15}N-labeled compound is assigned to the antisymmetric stretch $\nu(CN)_{as}$ (band III). This mode corresponds to ν_{26} in free piperidine (vide supra). The band at 1208 cm^{-1} that shifts to 1195 cm^{-1} in the isotope-labeled complex is assigned to band IV, which is a combination of ν(NN) with the H−C−H twisting mode ν_{25}. A mixture of ν(NN) with ν_{28} is assigned to the band at 1121 cm^{-1} (band V), shifting to 1111 cm^{-1} upon isotopic substitution. In the Raman spectra of $\mathbf{B}^W$, these features and their isotopic shifts are observed as well (cf. Figure S2 and Table 4).

Table 4. Observed and Calculated Frequencies for $^{14}N-\mathbf{B}^W$ and $^{15}N-\mathbf{B}^W$

band no.	main character	exptl IR ^{14}N	exptl IR ^{15}N	exptl Raman ^{14}N	exptl Raman ^{15}N	QCB-NCA ^{14}N	QCB-NCA ^{15}N	DFT
I	ν(NN) + ν_{19}: $\boldsymbol{\nu(NN)^1}$	1382	1366			1379	1364	1391
II	ν_{21}	1329	1321			1329	1324	1372
III	$\boldsymbol{\nu(CN)_{as}}$	1237	1223	1236	1228	1242	1230	1270
IV	ν(NN) + ν_{25}: $\boldsymbol{\nu(NN)^2}$	1208	1195	1203	1184	1214	1204	1243
V	ν(NN) + ν_{28}: $\boldsymbol{\nu(NN)^3}$	1121	1111	1123	1112	1125	1120	1153
VIa	ν_{35} + ν(WN)	873	867	878	876	865	860	876
VIb	ν_{38} + ν(WN)	813	807	813	806	804	797	812
VII	ν_{39} + ν(WN)	663	657			635	626	644
VIIIa	δ^{ip}(WNN)	554	541	554	542	557	544	576
VIIIb	δ^{oop}(WNN)	526	516			527	513	500
IX	ν_{40} + ν(WN)	496	493			483	481	495

By analogy to $\mathbf{A}^W$, two isotope-sensitive features are found in the region between 900 and 800 cm^{-1}. In this spectral range, the piperidine ring vibrations ν_{35}/ν_{38} are located. Features at 873 and 813 cm^{-1} correspond to bands VIa and VIb, respectively. The band at 663 cm^{-1} that shifts to 657 cm^{-1} in the ^{15}N-labeled compound is assigned to a combination of ν_{39} with ν(WN) (band VII). At 554 cm^{-1}, the spectrum of $^{14}N-\mathbf{B}$ exhibits a peak that shifts about -13 cm^{-1} in the spectrum of $^{15}N-\mathbf{B}^W$ to 541 cm^{-1} and is assigned to the bending mode δ^{ip}(WNN) (VIIIa). The second (out-of-plane) component of δ(WNN), VIIIb, is found again in the FIR region. This mode is associated with the band at 526 cm^{-1} that shifts to 516 cm^{-1} in the spectrum of the isotope-labeled complex. The feature at 496 cm^{-1} (IX), finally, shows a shift to 493 cm^{-1} on isotopic substitution and belongs to a combination of ν_{40} with ν(WN).

Scheme 2. Structure of Model System **A′** (Central Core) along with Labeling of Internal Coordinates

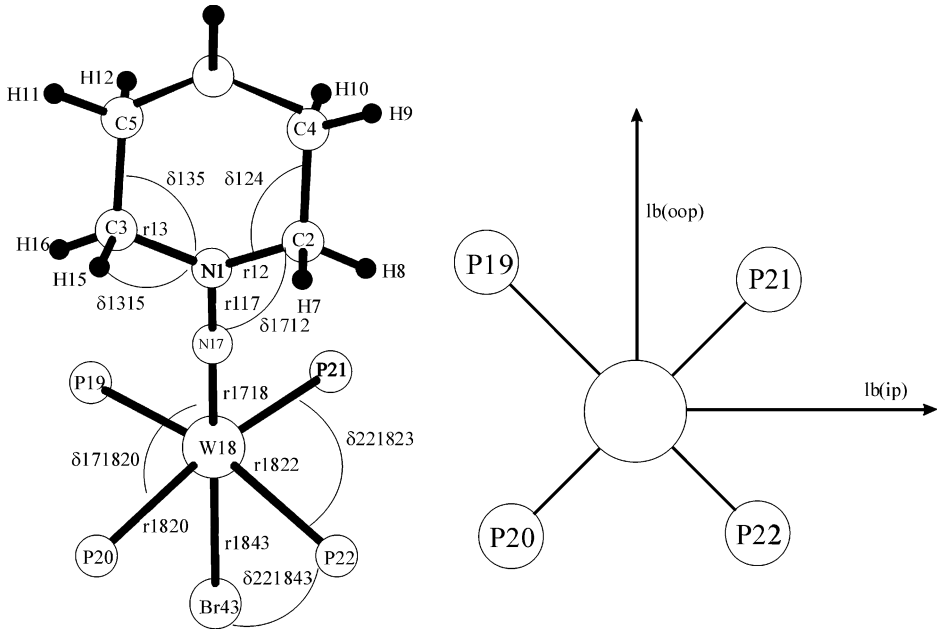

Scheme 3

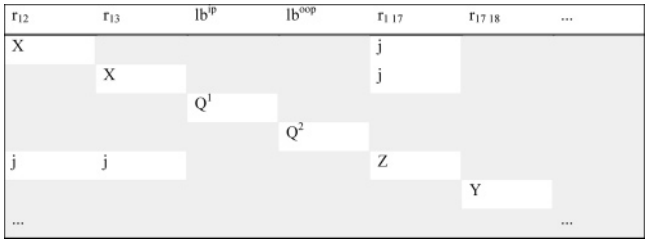

Table 5. Force Constants for [WBr(NNC$_5$H$_{10}$)(dppe)$_2$]Br (**A**^{W})

force constant	type	QCB-NCA	DFT
Y	WN	5.73	5.93
Z	NN	6.95	7.76
X	CN	3.64	3.54
Q^1	WNN	0.62	0.57
Q^2	WNN	0.34	0.40
j	CN/NN	0.26	0.36

4. Normal Coordinate Analysis of A^W. Normal coordinate analysis is carried out on a simplified model **A′** of **A**^{W}, as described in the Experimental and Computational Procedures section. Scheme 2 shows the central unit of **A′** including the labeling of internal coordinates. The structure of the *f* matrix is given in Scheme 3; force constants of the coordinates involved in the fitting procedure (N−N, C−N, W−N, and W−N−N) including the corresponding off-diagonal elements are collected in Table 5. Force constants for H−C−H and H−C−C/H−C−N bends have been reduced by 10 and 5% as in the case of piperidine. After NCA, a value of 6.95 mdyn/Å is obtained for the N−N force constant *Z*; for the W−N force constant, a value of 5.73 mdyn/Å results. The C−N force constant *X* is determined to be 3.64 mdyn/Å. In the course of the NCA procedure, the NN/CN off-diagonal element *j* is fitted to 0.26 mdyn/Å. For the in-plane and out-of-plane bending vibrations of the WNN unit, force constants of 0.62 and 0.34 mdyn·Å are obtained. The distribution of the potential energy (PED) is shown in Table 6. Eigenvectors of important vibrations are shown in Figure 6.

Because of strong coupling of the N−N stretch with H−C−H bending motions, ν(NN) is split into three modes, I, IV, and V. The main component I is a combination of ν(NN) (46%) with ν_{12} of the piperidine ring ($\nu(NN)^1$) (cf. Figure 6). NCA does not reproduce the splitting of this mode into bands Ia and Ib and leads to a value of 1416 cm^{-1} for ^{14}N−**A**^{W} with an isotopic shift of −27 cm^{-1}, in good agreement with the combined shifts observed for bands Ia and Ib. The second component of the N−N stretch is a combination of ν(CN) and ν_{25} ($\nu(NN)^2$, band IV), which is observed at 1236 cm^{-1} (^{14}N−**A**) and calculated by NCA at 1236 cm^{-1}. Band V ($\nu(NN)^3$), which is observed at 1125 cm^{-1} with an isotope shift of about −5 cm^{-1}, is attributed to ν_{28} admixed with 6% ν(NN) and 4% WN. NCA leads to a frequency of 1135 cm^{-1} with an isotopic shift of −3 cm^{-1}. The antisymmetric C−N stretching vibration $\nu(CN)_{as}$ is observable only for ^{15}N−**A**^{W} at 1258 cm^{-1}; the corresponding feature in the spectrum of ^{14}N−**A**^{W} is possibly masked by a band at 1270 cm^{-1}. Normal coordinate analysis leads to a frequency of 1271 cm^{-1} with an isotope shift to 1268 cm^{-1} for this vibration. In the region from 800 to 900 cm^{-1}, piperidine ring vibrations ν_{35} and ν_{38} are located. Bands VIa and VIb are assigned to ν_{35} and ν_{38}, which are admixed with 55 and 15% WN, respectively. These two vibrations are calculated with NCA procedure at 865 and 804 cm^{-1}. (The experimental values were 874 and 820 cm^{-1}.)

The metal−N stretching vibration is distributed over multiple bands, which makes an unequivocal assignment difficult. The W−N force constant *Y* is therefore only slightly modified with respect to the DFT result and set to 5.73 mdyn/Å. The bending vibrations of the linear W−N−N unit are split into the two orthogonal components labeled δ^{ip} and δ^{oop}. The feature in the spectrum of ^{14}N−**A**^{W} at 585 cm^{-1} that shifts to 572 cm^{-1} in the spectrum of ^{15}N−**A**^{W} is assigned

Table 6. Potential-Energy Distribution for $[WBr(NNC_5H_{10})(dppe)_2]Br$ ($\mathbf{A}^W$)

	no.	PED
$\nu(NN) + \nu_{12}$: $\boldsymbol{\nu(NN)^1}$	I	46% NN, 18% HCH, 10% WN, 9% HCC, 4% NCH, 3% CN, 3% NCC
$\nu_{21} + \nu(NN) + \nu(CN)$	II	45% HCC, 19% HCN, 14% CC, 2% NN, 1% CN
$\nu_{24} + \nu(NN) + \nu(CN)_{as}$	III	57% HCC, 24% HCN, 8% CC, 2% NN, 2% CN
$\nu_{25} + \nu(NN)$: $\boldsymbol{\nu(NN)^2}$	IV	41% HCC, 28% HCN, 14% NN, 6% WN, 4% CN
$\nu_{28} + \nu(NN)$: $\boldsymbol{\nu(NN)^3}$	V	36% HCC, 27% HCN, 8% CC, 6% NN, 4% WN, 4% τCC
$\nu_{35} + \nu(WN)$	VIa	55% WN, 41% CC, 30% CN, 5% HCC, 2% HCN, 2% CNC, 2% NNC, 2% CCC
$\nu_{38} + \nu(WN)$	VIb	37% CC, 27% CN, 15% WN, 6% HCC, 4% τCC, 2% HCN
ν_{39}	VII	12% CN, 3% NN, 5% WN, 39% HCC, 3% NNC, 9% NCC, 2% HCN
$\delta^{ip}(WNN)$	VIIIa	38% NNC, 24% lb^{ip}, 10% CN, 5% CC, 5% NWP, 4% PC, 3% lb^{oop}, 2% lb^{NWBr}
$\delta^{oop}(WNN)$	VIIIb	66% lb^{oop}, 12% NWP 3%, lb^{NWBr}, 2% lb^{ip}, 2% WN, 2% τCC
$\nu_{40} + \nu(WN)$	IX	37% CCC, 31% HCC, 10% τCC, 9% WN, 5% CN, 2% NN

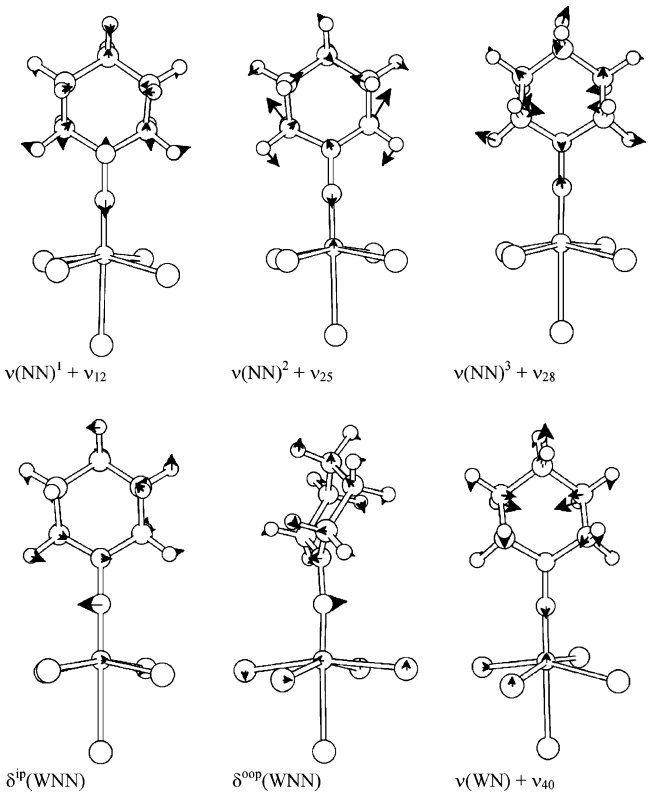

Figure 6. Calculated ν(NN), ν(WN), and δ(WNN) vibrations for $\mathbf{A}'$.

to δ^{ip}(WNN). The resulting force constant (Q^1) is determined to be 0.62 mdyn·Å, corresponding to a frequency of 587 cm^{-1} for the in-plane vibration. Analysis of the PED shows that NNC− (38%) bending modes make a large contribution to this mode. The corresponding out-of-plane component is determined by NCA to be 521 cm^{-1}; the resulting force constant is 0.34 mdyn·Å. With an isotope shift of −2 cm^{-1}, a combination of ν_{40} with ν(WN) (2%) is observed at 492 cm^{-1}; NCA gives a value of 483 cm^{-1} with an isotopic shift to 481 cm^{-1}.

5. Normal Coordinate Analysis of $\mathbf{B}^W$. Normal coordinate analysis for $\mathbf{B}^W$ is performed on model complex $\mathbf{B}'$ as described in the Experimental and Computational Procedures section. Scheme 4 shows the central unit of **B'** including the internal coordinate labeling. The structure of the *f* matrix is identical to that of $\mathbf{A}^W$, except for the absence of the coordinates associated with the bromo ligand. The force constants for the H−C−H and H−C−C/H−C−N bends are reduced by 10 and 5%, respectively, as was done for piperidine. The force constants for C−N, N−N stretching, and W−N−N bending vibrations are refined as described for compound $\mathbf{A}^W$ and collected in Table 7. Off-diagonal elements between internal coordinates CN and NN were not fitted and set to the DFT value. Table 8 presents the potential energy distribution (PED); eigenvectors of important vibrations are given in Figure 7. For the N−N force constant *Z*, a value 6.4 mdyn/Å is obtained; the C−N force constant *X* is determined to be 3.52 mdyn/Å. The off-diagonal element *j* between the two coordinates is set to 0.38 mdyn/Å.

Because of the coupling of the N−N stretching vibration with the H−C−H bending modes of the piperidine fragment, ν(NN) is split into three vibrations (I, IV, and V). Mode I ($\nu(NN)^1$) is a combination of ν(NN) with ν_{19} of piperidine, exhibiting 39% NN and 9% WN character. NCA predicts a frequency of 1379 cm^{-1} with an isotope shift to 1364 cm^{-1}. For band IV ($\nu(NN)^2$), which is observed at 1208 cm^{-1}, shifting to 1195 cm^{-1} on isotopic substitution, NCA gives a frequency of 1214 cm^{-1} with a shift to 1204 cm^{-1}. This mode has 24% NN−, 9% HCN−, and 50% HCC contributions. The third component of the N−N stretch ($\nu(NN)^3$, band V) is a combination with 42% HCC and 37% HCP of the phosphine ligand, observed at 1121 cm^{-1} ($^{14}N-\mathbf{B}^W$) and 1111 cm^{-1} ($^{15}N-\mathbf{B}^W$; IR). N−N and W−N contribute 3 and 1%, respectively, to this vibration, which is calculated by NCA at 1125 cm^{-1} with an isotope shift of −5 cm^{-1}.

Band III corresponds to ν_{26} in free piperidine with 38% CN contribution and a large participation of HCC (39%). This vibration is observed at 1237 cm^{-1} for $^{14}N-\mathbf{B}^W$ and 1223 cm^{-1} for $^{15}N-\mathbf{B}^W$; NCA gives values of 1242 and 1230 cm^{-1}, respectively. In the region between 800 and 900 cm^{-1}, vibrations of the piperidine ring (ν_{35} and ν_{38}) are located. For these modes, frequencies of 865 and 804 cm^{-1} are determined by NCA; upon isotopic substitution, values of 860 and 797 cm^{-1} result (bands VIa and VIb). In the IR spectra, a band is observed at 873 cm^{-1} that shifts to 867 cm^{-1} in the spectra of the isotope-labeled compound; an additional band exhibiting an isotope shift is found at 813 cm^{-1} (^{15}N: 807 cm^{-1}).

The metal−N stretching vibration is distributed over several modes, which makes a determination of the W−N force constant *Y* difficult. *Y* is therefore not modified from the DFT value and is set to 4.87 mdyn/Å. The peak observed at 554 cm^{-1} that shifts to 541 cm^{-1} in the spectrum of $^{15}N-\mathbf{B}^W$ is assigned to δ^{ip}(WNN). The corresponding force constant Q^1 is determined to be 0.25 mdyn·Å, leading to a calculated frequency of 557 cm^{-1} with an isotope shift to

Scheme 4. Structure of Model System **B′** (central core) along with Labeling of Internal Coordinates

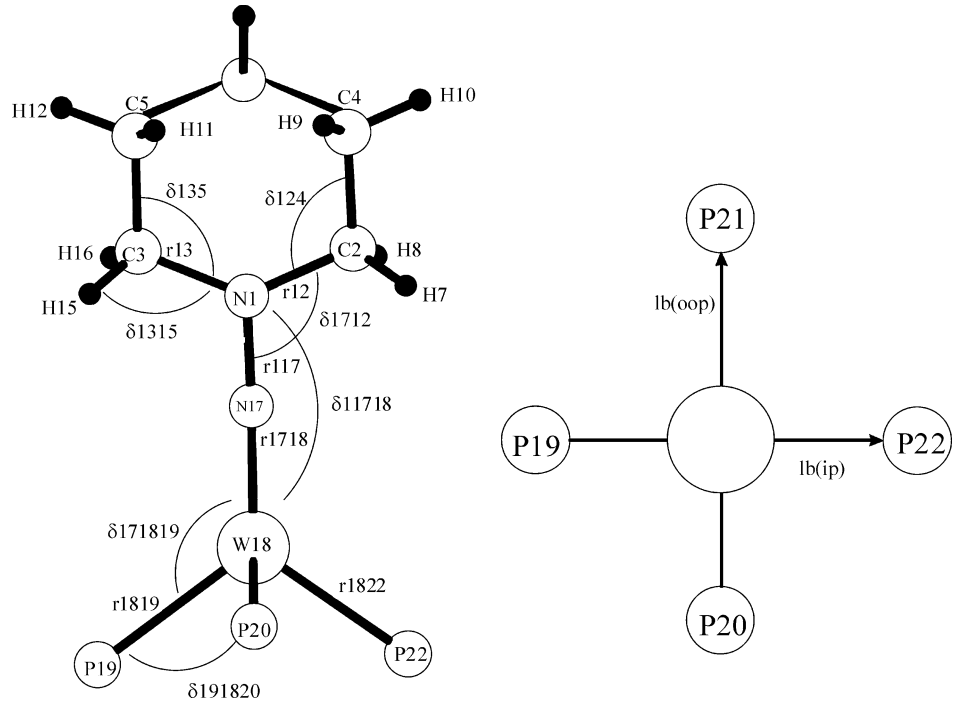

Table 7. Force Constants for $[W(NNC_5H_{10})(dppe)_2]$ ($\mathbf{B}^W$)

force constant	type	QCB-NCA	DFT
Y	WN	4.87	4.87
Z	NN	6.4	6.50
X	CN	3.52	3.69
Q^1	WNN	0.25	0.31
Q^2	WNN	0.58	0.31
j	CN/NN	0.38	0.38

544 cm^{-1}. Analysis of the potential energy distribution shows that NNC makes a large contribution (47%) to this mode. For the δ^{oop} component, a force constant of 0.58 mdyn·Å is determined by NCA, leading to a vibrational frequency of 527 cm^{-1} with an isotope shift to 513 cm^{-1}. With a shift of about -3 cm^{-1}, a combination of ν_{40} and ν(WN) is observed at 496 cm^{-1}. NCA determines a value of 483 cm^{-1} with a shift to 481 cm^{-1} in the ^{15}N-labeled complex for this mode.

C. Electronic Structure of $\mathbf{A}^W$ and $\mathbf{B}^W$. Models and Geometry Optimizations. The electronic structure of compounds $\mathbf{A}^W$ and $\mathbf{B}^W$ is analyzed on the basis of models of the corresponding molybdenum compounds $\mathbf{A}^{Mo}$ and $\mathbf{B}^{Mo}$, $[MoBr(NNC_5H_{10})(PH_2C_2H_4PH_2)_2]^+$ (**Ã**) and $[Mo(NNC_5H_{10})(H_2PC_2H_4PH_2)_2]$ (**B̃**), respectively, which are shown in Figure 8. In both structures, the phenyl rings of the dppe ligands are substituted by hydrogen atoms. The structural parameters of the model obtained by geometry optimization (B3LYP/LANL2DZ) are collected in Table 9 and compared with the structural data of related systems. The calculated N−N distance (1.31 Å) is comparable to that of the established hydrazido(2-) complexes.[22] The W−N distance (1.78 Å) is as large as that in the crystal structure of compound $\mathbf{B}^W$; that is, it is larger than that for ordinary hydrazido(2-) systems (vide supra). The metal phosphine distances are 2.56 Å, the W−Br bond length is 2.72 Å, and the resulting angle of the W−N−N unit is 178.3°. The N−N(C)−C unit is not planar, in contrast to the N−N−H_2 unit of the Mo−NNH_2 model system $[MoF(NNH_2)(PH_3)_4]^+$.[2a]

The structure of model complex $[Mo(NNC_5H_{10})(H_2PC_2H_4PH_2)_2]$ (**B̃**) is based on the crystal structure of $\mathbf{B}^W$ followed by geometry optimization (B3LYP/LANL2DZ) (cf. Figure 8). The resulting structural parameters are collected in Table 9. The N−N distance of the optimized complex (1.34 Å) is larger than that calculated for model **Ã** but somewhat smaller than that found by X-ray analysis for compound $\mathbf{B}^W$ (1.388 Å). The metal−N distance of the model system, in contrast, is longer (1.82 Å) than that observed in the crystal structure (1.781 Å, vide supra). The W−N−N angle is 178.7° (exptl value: 177.8°), and W−P bond lengths are found in a range between 2.49 and 2.51 Å, slightly longer than what was observed. In the crystal structure as well as in the optimized complex, the N−N(C)−C unit is again nonplanar, indicating some sp^3 character of the terminal N atom.

D. Electronic Structure of $[MoBr(NNC_5H_{10})(H_2PCH_2CH_2PH_2]Br$ (Ã). The MO diagram of model **Ã** is shown in Figure 8. Figure 9 gives the contour plots of important molecular orbitals, and orbital decompositions are collected in Table 10. The HOMO is the nonbonding orbital d_{xy} with 75% metal contribution. Below the HOMO are the bonding combinations of d_{xz} and d_{yz} with the π^*_v and π^*_h orbitals of the NNC_5H_{10} group, respectively, where v and h refer to the orientation of these π* orbitals with respect to the $N_\alpha R_2$ plane (v = vertical, h = horizontal). As outlined before, the π^*_h orbital of N_2 acquires p lone pair character at N_α upon double protonation/alkylation at N_β; the corresponding bonding combination ⟨61⟩ is denoted π^*_h_d_{yz}. The π^*_v orbital of N_2 more or less retains its π* character at the NNH_2/NNR_2 stage and interacts with d_{xz} in a back-bonding fashion; the corresponding bonding combination ⟨66⟩ is denoted π^*_v_d_{xz}. Metal−N σ bonding is mediated by p_σ_d_{z^2}. The HOMO−

Table 8. Potential-Energy Distribution for $[W(NNC_5H_{10})(dppe)_2]$ ($\mathbf{B}^W$)

	no.	PED
ν(NN) + ν_{19} : $\boldsymbol{\nu(NN)^1}$	I	39% NN, 24% HCN, 22% HCC, 9% WN, 2% CC, 2% HCH
ν_{21}	II	68% HCC, 29% HCN, 2% NNC
$\boldsymbol{\nu(CN)_{as}}$	III	39% HCC, 38% CN, 6% NNC, 6% CC, 2% HCN, 4% CCC, 2% NCC, 2% tCC
ν(NN) + $\nu_{25}\boldsymbol{\nu(NN)^2}$	IV	50% HCC, 24% NN, 9% HCN, 8% WN, 3% CC, 2% CCC
ν(NN) + ν_{28}: $\boldsymbol{\nu(NN)^3}$	V	42% HCC (phos), 37% HCP, 6% HCN, 3% NN, 3% HCC, 1% WN
ν_{35} + ν(WN)	VIa	45% CC, 28% CN, 8% WN, 6% HCC, 2% HCN, 2% NNC, 2% CNC, 2% CCC
ν_{38} + ν(WN)	VIb	43% CC, 31% CN, 17% WN, 3% HCC, 3% tCC, 2% HCN
ν_{39} + ν(WN)	VII	30% HCC, 20% HCN, 10% CN, 10% WN, 9% NNC, 6% lb^{oop}, 5% NN, 2% CC, 2% CNC, 2% τ^{CC}
δ^{ip}(WNN)	VIIIa	47% NNC, 17% lb^{ip}, 10% NWP, 7% CN, 6% CC, 4%PC, 2% lb^{oop}
δ^{oop}(WNN)	VIIIb	62% lb^{oop}, 13% NWP, 5% WN, 3% CNC, 2% NNC, 2% HCC
ν_{40} + ν(WN)	IX	36% HCC, 30% CCC, 10% tCC, 9% WN, 4% CN, 2% NN

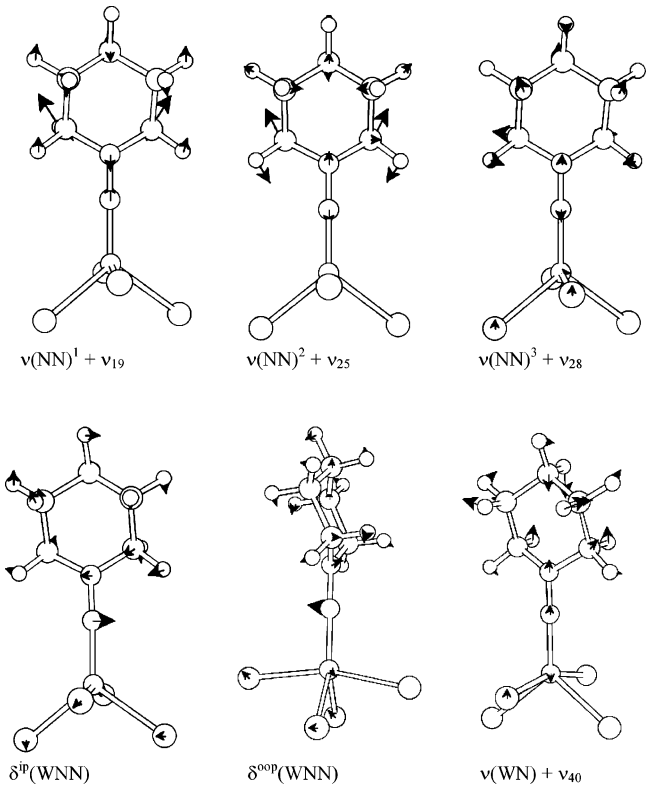

Figure 7. Calculated ν(NN), ν(WN), and δ(WNN) vibrations for $\mathbf{B}'$.

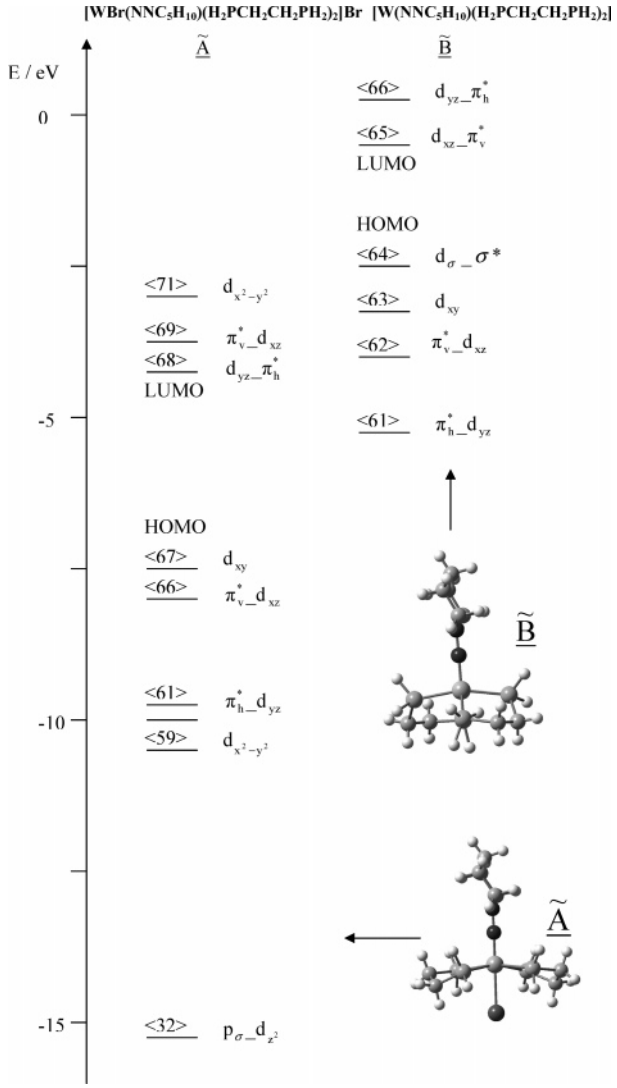

Figure 8. MO diagram of $\tilde{\mathbf{A}}$ and $\tilde{\mathbf{B}}$.

LUMO gap is 3.74 eV. The LUMO is the orbital ⟨68⟩ d_{yz}_π^*_h, which is the antibonding combination between d_{yz} and π^*_h and is of primary metal character. Orbital ⟨69⟩ is the π^*_v metal−ligand antibonding combination that has predominantly ligand character.

More information on the electronic structures of $\mathbf{A}^W$ and $\mathbf{B}^W$ can be obtained from a charge analysis. Of course, the actual charges depend on the type of applied method; in the present paper, NPA (natural population analysis) has been employed.[16] As is evident from Table 11, the N_β of $\tilde{\mathbf{A}}$ is more negatively charged (−0.23) than N_α (−0.15). The negative charge on N_β is comparable to that present in the Mo fluoro-NNH_2 model complex $[MoF(NNH_2)(PH_3)_4]^+$. This structure, however, has a positive charge on N_α. The negative charge on the metal (−0.28) in $\tilde{\mathbf{A}}$ is a consequence of the coordination of six strong donors: four phosphines, the NNC_5H_{10} group, and the bromo ligand. The phosphine atoms, in turn, being strong σ donors, acquire positive charges.

E. Electronic Structure of $[Mo(NNC_5H_{10})(H_2PCH_2CH_2PH_2]$ ($\tilde{\mathbf{B}}$). Figure 8 also contains the MO diagram of model system $\tilde{\mathbf{B}}$. Contour plots of important molecular orbitals are presented in Figure 10; orbital decompositions are given in Table 12. Model $\tilde{\mathbf{B}}$ is obtained from $\tilde{\mathbf{A}}$ by two-electron reduction and elimination of the bromo ligand. These two additional electrons are located in the HOMO of $\tilde{\mathbf{B}}$, which is a linear combination of a metal d_σ orbital with a ligand σ^* orbital.[26] It is labeled d_σ_σ^* and has 45% metal and 13% N−N character. Because of the missing trans ligand, this orbital has a large lobe toward the open face of

(26) The metal orbital is actually a hybrid of a d_{z^2} and a $d_{x^2-y^2}$ orbital.

Table 9. Structure of the Model Systems **Ã** and **B̃** and Comparison with the Crystal Structures of $\mathbf{B}^{W}$ and Related NNH_x Compounds ($x = 2, 3$)

	Δ(NN)	Δ(MN)	Δ(MP)	Δ(MX)	α(MNN)	ref
$[MoBr(NNC_5H_{10})(PH_2C_2H_4PH_2)_2]^+$	1.31	1.78	2.56	2.72	178.3	*a*
$[Mo(NNC_5H_{10})(PH_2C_2H_4PH_2)_2]$	1.34	1.82	2.49−2.51		178.7	*a*
$[W(NNC_5H_{10})(dppe)_2]$	1.39	1.78	2.39−2.47		177.8	*a*
$[MoF(NNH_2)(dppe)_2]^+$	1.332	1.763	2.54	1.99	176.4	*b*
$[WCl(NNH_2)(dppe)_2]^+$	1.37	1.73	~2.5	2.42	171.0	*b*
$[WF(NNH_2)(depe)_2]^+$	1.355	1.771	~2.5	2.027	175.0	*c*
$[WCl(NNH_3)(PMe_3)_4]^{2+}$	1.396	1.785	2.519	2.463	179.2	*d*

[a] This work. [b] Hidai, M.; Kodama, T.; Sato, M.; Harakawa, M.; Uchida, Y. *Inorg. Chem.* **1976**, *15*, 2694. [c] Barclay, J. E.; Hills, A.; Hughes, D. L.; Leigh, G. J.; Macdonald, C. J. *J. Chem. Soc., Dalton Trans.* **1990**, 2503. [d] Galindo, A.; Hills, A.; Hughes, D. L.; Richards, R. L. *J. Chem. Soc., Dalton Trans.* **1990**, 283.

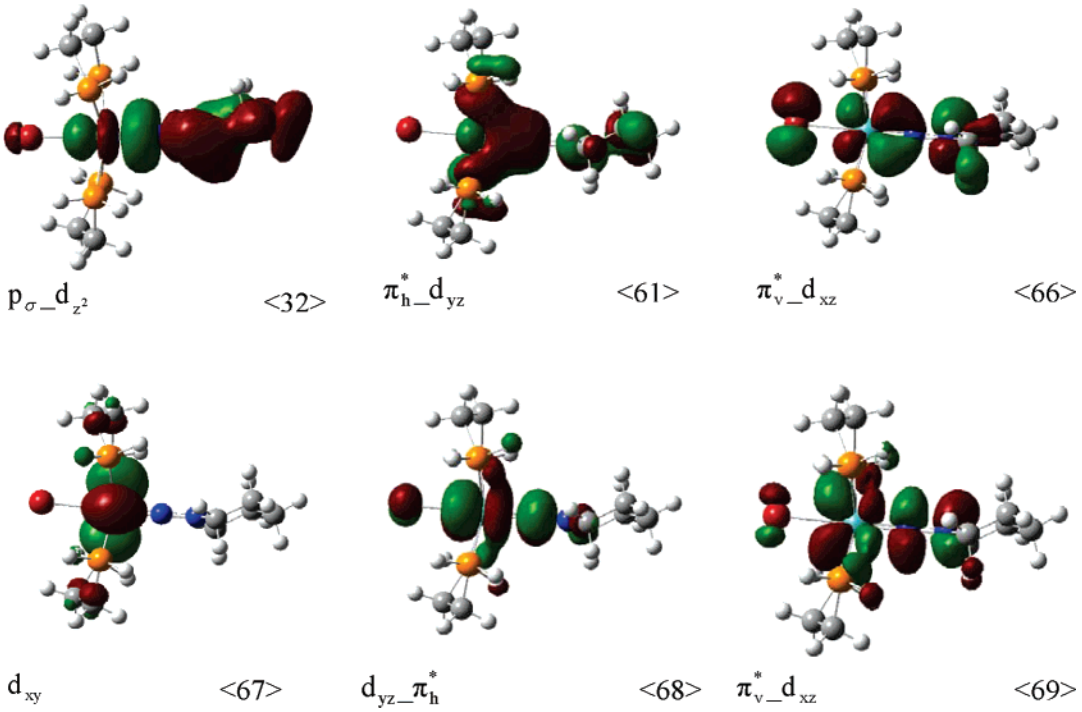

Figure 9. Contour plots of important orbitals of $[WBr(NNC_5H_{10})(H_2PCH_2CH_2PH_2)_2]Br$.

Table 10. Charge Decomposition and Energies for Important Molecular Orbitals of $[MoBr(NNC_5H_{10})(H_2PC_2H_4PH_2)_2]^+$ (**Ã**)

			orbital decompositions							
orbital	no.	energy (eV)	$\%N_\alpha$	$\%N_\beta$	%Mo	%P	%HP	%Br	$\%C_5H_{10}$	$\%C_4H_8$
$d_{x^2-y^2}$	⟨71⟩	−3.30	1	1	34	53	4	1	1	7
π^*_v–d_{xz}	⟨69⟩	−4.17	27	13	29	13	6	3	7	2
d_{yz}–π^*_h	⟨68⟩	−4.78	21	0	48	9	5	3	13	2
d_{xy}	⟨67⟩	−8.52	0	0	75	3	4	0	0	18
π^*_v–d_{xz}	⟨66⟩	−8.74	5	35	32	0	1	13	12	0
d_{yz}–π^*_h	⟨62⟩	−11.05	8	2	18	41	6	10	7	10
π^*_h–d_{yz}	⟨61⟩	−11.14	32	6	15	18	3	0	26	2
$d_{x^2-y^2}$	⟨59⟩	−11.65	0	0	25	39	1	0	0	35
p_σ–d_{z^2}	⟨32⟩	−17.03	39	18	13	0	0	1	28	0

the complex. The two electrons of this orbital are involved in the heterolytic cleavage of the N−N bond, which is considered in more detail in the following paper.

The nonbonding orbital d_{xy} (HOMO−1), which is the HOMO of the octahedral precursor $\mathbf{A}^{W}$ (vide supra), has 59% metal contribution. At lower energy, the bonding combinations of d_{yz} and d_{xz} with π^*_v and π^*_h, respectively, are found (vide supra). These are the molecular orbitals π^*_v_d_{xz} ⟨62⟩ and π^*_h_d_{yz} ⟨61⟩. Orbital ⟨61⟩ has only 9% metal contribution and 54% ligand character with the main contribution coming from N^α (51%); orbital ⟨62⟩ has 33% metal and 43% π^* contributions, mainly contributed by N^β. The antibonding combinations of the π^* orbitals with metal d orbitals (⟨65⟩ and ⟨66⟩) have higher metal character and only a small amount of N−N ligand contribution. Thus, the LUMO is d_{xz}_π^*_v with 27% metal contribution and 12% ligand π^* character, whereas the LUMO + 1 d_{yz}_π^*_h has only 6% π^* character and 23% metal contribution.

As is evident from Table 11, the negative charges on the metal, N_α and N_β, have increased in **B̃** as compared to those in **Ã.** In **B̃**, the charge on N_α (−0.36) is more negative than that on N_β (−0.26), which is in contrast to **Ã** (N_α −0.15, N_β

Table 11. NPA Charges for $\tilde{\mathbf{A}}$, $\tilde{\mathbf{B}}$, and Related Models

compound	NPA charge Mo	N_α	N_β	X	P	ref
$[MoBr(NNC_5H_{10})(PH_2C_2H_4PH_2)_2]^+$	−0.28	−0.15	−0.23	−0.45	1.84	*a*
$[Mo(NNC_5H_{10})(PH_2C_2H_4PH_2)_2]$	−0.52	−0.36	−0.26		1.72	*a*
$[MoF(NNH_2)(PH_3)_4]^+$	+0.04	−0.21	−0.68	−0.55	0.96	*b*
$[MoF(NNH_3)(PH_3)_4]^{2+}$	0.19	−0.36	−0.60	−0.44	0.77	*c*

[a] This work. [b] Lehnert, N.; Tuczek, F. *Inorg. Chem.* **1999**, *38*, 1671. [c] Horn, K. H.; Lehnert, N.; Tuczek, F. *Inorg. Chem.* **2003**, *42*, 1076.

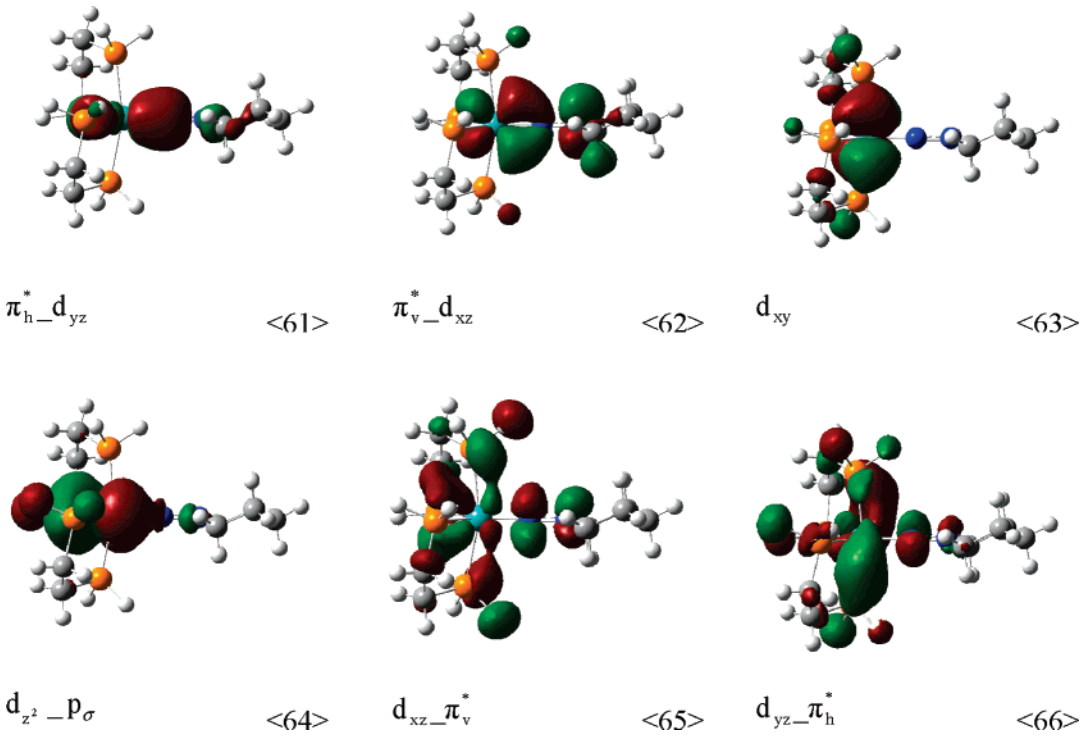

Figure 10. Contour plots of important orbitals of $[W(NNC_5H_{10})(H_2PCH_2CH_2PH_2)_2]$.

Table 12. Charge Decomposition and Energies for Important Orbitals of $[Mo(NNC_5H_{10})(PH_2C_2H_4PH_2)_2]$ ($\tilde{\mathbf{B}}$)

orbital	no.	energy (eV)	orbital decompositions %N_α	%N_β	%Mo	%P	%H^p	%C_5H_{10}	%C_4H_8
d_{yz}–π^*_h	⟨66⟩	0.39	5	1	23	24	21	3	23
d_{xz}–π^*_v	⟨65⟩	−0.49	8	4	27	24	9	5	23
d_σ–σ^*	⟨64⟩	−2.92	8	5	45	9	23	1	8
d_{xy}	⟨63⟩	−3.64	1	0	59	8	12	0	29
π^*_v–d_{xz}	⟨62⟩	−4.47	9	34	33	3	4	12	4
π^*_h–d_{yz}	⟨61⟩	−5.83	52	2	9	12	1	20	2
$d_{x^2-y^2}$	⟨59⟩	−7.41	2	0	16	56	3	0	23
p_σ–d_{z^2}	⟨40⟩	−11.05	21	17	8	1	1	47	2

−0.23). This is attributed to the accumulation of negative charge on the metal (charge −0.52) in $\tilde{\mathbf{B}}$. The increased negative charges on the tungsten atom and N_α possibly contribute to the elongation of the metal−N bond in $\mathbf{B}^W$ as compared to that in $\mathbf{A}^W$ (see below).

IV. Discussion

The investigations presented in this paper have lead to structural, spectroscopic, and theoretical characterization of the six-coordinate Mo/W alkylhydrazido complexes $\mathbf{A}^{Mo}/\mathbf{A}^W$ and their two-electron-reduced, five-coordinate derivatives $\mathbf{B}^{Mo}/\mathbf{B}^W$. These compounds are relevant to the area of nitrogen fixation because protonation of $\mathbf{B}^W$ leads to N−N cleavage under the formation of the nitrido or imido complex and piperidine. This process is analogous to the splitting of the N−N bond in Mo and W hydrazidium (NNH_3^-) complexes, which is involved in the reduction and protonation of molecular dinitrogen. Use of alkylated instead of protonated derivatives of Mo/W N_2 complexes for the investigation of N−N cleavage allows one to avoid the problems associated with the acidity of Mo/W NNH_2 and NNH_3 systems.

Splitting of the N−N bond generating the first molecule of NH_3 completes the first part of the reduction and protonation of N_2 mediated by Mo/W diphosphine complexes; in the second part of the reactive cycle, the nitrido or imido complex is protonated and reduced to generate another molecule of NH_3 and a Mo/W complex that is capable of rebinding N_2. The most difficult step of the entire cycle involves the very first protonation of bound N_2 leading to the NNH^- species, which requires the "activation" of N_2, that is, the transfer of electronic charge from the metal to the ligand. As inferred from vibrational spectroscopy, the bond order of N_2 is thereby reduced from ∼3 to ∼2.[3] The double-bond character of the NNH^- ligand is not significantly altered by protonation to the NNH_2 intermediate. Further protonation leads to the Mo(IV)/W(IV) NNH_3 (hydrazidium) complex, which has a strong N−N single bond

(and a force constant of 6.03 mdyn/Å). More importantly, this bond is stable with respect to N−N cleavage for Mo/W complexes with diphosphine coligands; that is, without two-electron reduction by an external reductant, the N_2 chemistry of these systems stops at this point.[3c]

The N−N cleavage reaction at the level of two-electron-reduced Mo/W NNH_3 complexes with diphosphine ligands can be studied conveniently on the basis of the NNR_2 complexes $\mathbf{A}^{Mo}/\mathbf{A}^{W}$ ($NR_2 = NC_5H_{10}$). This study focuses on the tungsten complex $[WBr(NNC_5H_{10})(dppe)_2]Br$ ($\mathbf{A}^{W}$), which can be two-electron reduced with BuLi, generating under the loss of Br^- the five-coordinate complex $[W(NNC_5H_{10})(dppe)_2]$ ($\mathbf{B}^{W}$). Protonation of $\mathbf{B}^{W}$ leads to the dialkylhydrazidium ($NNHR_2$) intermediate $[W(NNHC_5H_{10})(dppe)_2]$ that spontaneously cleaves the N−N bond, generating the W(IV) nitrido complex $[W(N)(dppe)_2]^+$ and HNC_5H_{10} (piperidine). The crystal structure of $\mathbf{B}^{W}$ indicates a geometry between square pyramidal and trigonal bipyramidal with the NNC_5H_{10} group in the apical position and in the trigonal plane, respectively. The temperature-dependent ^{31}P NMR spectra of $\mathbf{B}^{Mo}$ indicate that this geometry is retained in solution. At room temperature, a rapid Berry pseudorotation between the axial and equatorial ligand positions takes place, giving rise to a singlet. This exchange process becomes slow at 203 K, generating two signals that are separated by ∼1 Hz. At 1.39 Å, the N−N distance of $\mathbf{B}^{W}$ is larger than that found in the W(IV) NNH_2 complex $[WF(NNH_2)(dppe)_2](BF_4)$ (1.36 Å) and equal to that observed in the W(IV) NNH_3 complex $[WCl(NNH_3)(PMe_3)_4]Cl_2$, where the N−N bond is found to be a short single bond (Table 9).[21] This agrees with the distinctly nonplanar geometry around the terminal nitrogen (N_β) in $\mathbf{B}^{W}$, which reflects significant sp^3 character at this atom. The metal−N distance of $\mathbf{B}^{W}$ is determined to be 1.78 Å, which is between the values observed for $[WF(NNH_2)(dppe)_2](BF_4)$ (1.77 Å) and $[WCl(NNH_3)(PMe_3)_4]Cl_2$ (1.79 Å).

More information on the electronic structure has been obtained by vibrational spectroscopy coupled to normal coordinate analysis (NCA). The vibrational spectra of both $\mathbf{A}^{W}$ and $\mathbf{B}^{W}$ show evidence for extensive mixing between the N−N and metal−N stretches on one hand and vibrations of the alkyl ring on the other hand, in particular, C−N stretches and HCC bends. The quantum chemistry-based normal coordinate analysis (QCB-NCA) has been applied to evaluate the experimental data. This method generates the initial guess of the *f* matrix by DFT methods.[3b] In a subsequent fitting procedure, the force constants are adjusted to match the observed frequencies. Specifically, this procedure allows one to fit those force constants that correspond to vibrations that have been assigned by isotope substitution, leaving all others at their values predicted by DFT. This generates a theoretically derived force field calibrated by experimental results. On the basis of this approach, the spectra of $\mathbf{A}^{W}$ and $\mathbf{B}^{W}$ have been fully analyzed. The force constants determined for the alkylated complexes $\mathbf{A}^{W}$ and $\mathbf{B}^{W}$ were found to fit within the systematics established for the NNH_x systems (Table 13).

Table 13. Force Constants $\mathbf{A}^{W}$, $\mathbf{B}^{W}$, and Related NNH_x Compounds

f(NN)	f(NN)	f(MN)	f(MNN)	ref
$[WBr(NNC_5H_{10})(dppe)_2]Br$	6.95	5.73	0.62/0.34	[a]
$[W(NNC_5H_{10})(dppe)_2]$	6.40	4.87	0.25/0.58	[a]
$[WF(NNH_2)(dppe)_2](BF_4)$	7.20	6.31	0.39/0.69	[b]
$[MoCl(NNH_2)(depe)_2]Cl$	7.16	5.52	0.38/0.67	[c]
$[WF(NNH_3)(depe)_2](BF_4)_2$	6.03	7.31	0.65	[d]
$[MoF(NNH_3)(depe)_2](BF_4)_2$	6.03	8.01	0.63	[d]

[a] This work. [b] Lehnert, N.; Tuczek, F. *Inorg. Chem.* **1999**, *38*, 1659. [c] Tuczek, F.; Horn, K. H.; Lehnert, N. *Coord. Chem. Rev.* **2003**, *245*, 107. [d] Horn, K. H.; Lehnert, N.; Tuczek, F. *Inorg. Chem.* **2003**, *42*, 1076.

For the parent compound $\mathbf{A}^{W}$, an N−N force constant of 6.95 is obtained, which is close to the values of Mo and W NNH_2 complexes, allowing us to attribute N−N double-bond character to this complex. This is supported by DFT, which predicts an N−N bond length of 1.31 Å and a W−N bond length of 1.78 Å for $\mathbf{A}^{W}$, comparable to the calculated and experimentally observed bond lengths of W(IV) NNH_2 compounds that have an N−N double bond.[3b] The nonplanarity at N_β that is evidenced by the geometry optimization of $\mathbf{A}^{W}$ thus appears to be induced by the cyclic structure of the alkyl substituent. The N−N force constant of $\mathbf{B}^{W}$ (6.4 mdyn/Å) is between the values found for the hydrazidium complexes $[MoF(NNH_3)(depe)_2](BF_4)_2$ and $[WF(NNH_3)(depe)_2](BF_4)_2$ (6.03 mdyn/Å) on one hand and Mo and W NNH_2 complexes (∼7.2 mdyn/Å) on the other hand, indicative of an intermediate position between an N−N double bond and an N−N single bond. The actual decrease of the N−N force constant upon going from $\mathbf{A}^{W}$ to $\mathbf{B}^{W}$ is therefore smaller than expected for the reduction of an N−N double bond to an N−N single bond.

The metal−N stretching force constant of $\mathbf{A}^{W}$ (5.73 mdyn/Å) is between the values found for Mo and W NNH_2 complexes (5.52 and 6.31 mdyn/Å, respectively) and is much smaller than that observed for Mo and W hydrazidium complexes (8.01 and 7.31 mdyn/Å, respectively), supporting the close relationship of $\mathbf{A}^{W}$ to corresponding NNH_2 systems. The fact that the metal−N bond in $\mathbf{A}^{W}$ is slightly weaker than that in the analogous W NNH_2 compound is attributed to the presence of a bromo ligand in the trans position, which is a stronger donor than fluoride present in the W NNH_2 system. Importantly, the metal−N force constant is reduced to 4.87 mdyn/Å in $\mathbf{B}^{W}$. This is in contrast to the protonation reactions of Mo/W N_2 complexes where the reduction of N−N bond order goes along with an increase of metal−N bond order.[3] A simultanenous elongation of the N−N and the metal−N bond upon two-electron reduction of $\mathbf{A}^{W}$ is also predicted by DFT, leading to an N−N bond length of 1.34 Å and a W−N bond length of 1.82 Å for $\mathbf{B}^{W}$ (calcd for $\mathbf{A}^{W}$ 1.31/1.78 Å; exptl for $\mathbf{B}^{W}$ 1.39/1.78 Å). The electronic structures of $\mathbf{A}^{W}$ and $\mathbf{B}^{W}$ have to be considered in more detail to understand these findings.

The MO scheme of $\mathbf{A}^{W}$ is closely related to that of Mo and W NNH_2 complexes. The dinitrogen π^* orbital in the NCC plane (π_h^*) has mostly lone pair character at N^α and interacts with the W d_{yz} orbital in a π-donor fashion, whereas the N−N out-of-plane orbital π_v^* interacts with the W d_{xz} orbital in a back-bonding manner. The HOMO of $\mathbf{A}^{W}$ is the

nonbonding d_{xy} orbital. The LUMO and LUMO + 1 are the antibonding combinations of π_h^* and π_v^* with the corresponding metal orbitals. Two-electron reduction of $\mathbf{A}^W$ leading to $\mathbf{B}^W$, however, does not populate these orbitals because the bromo ligand is lost in the course of this process. This causes a structural change from octahedral coordination to a geometry intermediate between square pyramidal and trigonal bipyramidal and entails significant electronic relaxation. In particular, a hybrid of d_{z^2} and $d_{x^2-y^2}$ (z along W−N−N) becomes the HOMO of the reduced derivative. This orbital, labeled d_{σ}_σ*, is metal−N σ bonded and contains an N−N antibonding interaction derived from the N−N σ* orbital. This is the major reason for the observation that the N−N bond strength is reduced in $\mathbf{B}^W$ as compared to that in $\mathbf{A}^W$. Because the metal−ligand interaction in this orbital is of mixed bonding−antibonding type, the reduction in metal−N bond strength upon two-electron reduction of $\mathbf{A}^W$ is probably not caused by population of this orbital but rather appears to be due to an increase of Coulomb repulsion between the metal and the ligand.

In conclusion, a full understanding of the electronic structure and the spectroscopic properties of complexes $\mathbf{A}^W$ and $\mathbf{B}^W$ has been achieved. Although the electronic properties and the geometric structures of $\mathbf{A}^W$ and $\mathbf{B}^W$ differ appreciably, their key relationship is the common phosphine ligation and the coordination of the NNC_5H_{10} ligand. Loss of the trans ligand is a consequence of the two-electron reduction of $\mathbf{A}^W$ and is characteristic of the Mo/W diphosphine systems; other systems mediate the same chemistry without this feature.[1] Two-electron reduction of $\mathbf{A}^W$ also leads to population of a d_{σ}-type HOMO, which is admixed with the N−N σ* orbital. Although this contribution is rather small (∼13%), it is sufficient to induce N−N cleavage after further protonation of $\mathbf{B}^W$ at N_{β}. In the following paper, it is shown that geometry optimization of the protonated $\mathbf{B}^W$ complex spontaneously leads to N−N bond cleavage, which is in agreement with the experimental observation. Because Mo(IV) hydrazidium compounds on one hand and two-electron-reduced NNH_2/NNR_2 compounds such as $\mathbf{B}^{Mo}$ and $\mathbf{B}^W$ on the other hand are inert to N−N cleavage, *both* two-electron reduction *and* protonation are required for this process. In particular, protonation of N_{β} lowers the N−N bond order even further, which lowers the σ* orbital in energy and acts to increase its contribution to the HOMO, thus facilitating N−N bond cleavage.

Acknowledgment. F.T. thanks DFG TU58-12 and FCI for funding this research.

Supporting Information Available: Raman spectra of [WBr(NNC$_5$H$_{10}$)(dppe)$_2$]Br, [WBr(^{15}N^{15}NC$_5$H$_{10}$)(dppe)$_2$]Br, [W(NNC$_5$H$_{10}$)(dppe)$_2$], and [W(^{15}N^{15}NC$_5$H$_{10}$)(dppe)$_2$] and data in CIF format. This material is available free of charge via the Internet at http://pubs.acs.org.

IC048675G